Mineralium Deposita (2020) 55:767–796
https://doi.org/10.1007/s00126-019-00939-8

ARTICLE

# Early Fimiston and late Oroya Au–Te ore, Paringa South mine, Golden Mile, Kalgoorlie: 4. Mineralogical and thermodynamic constraints on gold deposition by magmatic fluids at 420–300 °C and 300 MPa

Andreas G. Mueller[1] · Steffen G. Hagemann[1] · Joël Brugger[2] · Yanlu Xing[2] · Malcolm P. Roberts[3]

Received: 29 May 2019 / Accepted: 18 November 2019 / Published online: 30 January 2020
© Springer-Verlag GmbH Germany, part of Springer Nature 2020

## Abstract

The Golden Mile deposit (1767 t Au) in the Archean Yilgarn Craton, Western Australia, is controlled by D2 strike-slip and D3 reverse faults displacing folded tholeiitic greenstones. Granodiorite and monzodiorite dykes emplaced into the faults predate and are synchronous with propylitic and sericite–ankerite alteration overprinted by the ore. Arsenopyrite and chlorite thermometry and fluid-inclusion data indicate ore formation at 420 ± 30 °C and 300 MPa and cooling to the ambient temperature at 10 km depth (250–300 °C). Fimiston refractory ore (7 g/t Au) in propylitic Golden Mile Dolerite is zoned from inner albite–ankerite to outer ankerite–phengite–quartz replacement. Pyrite–magnetite is overprinted by pyrite–hematite ± anhydrite. Arsenical pyrite encloses chalcopyrite, tennantite, gold and tellurides. Gold thio-sulfide complexes, buffered by magmatic $SO_2$ and $H_2S$ in the fluid, were destabilised during the ankerite–pyrite replacement of propylitic chlorite, a reaction releasing hydrogen ions for the hydrolitic alteration of adjacent albite. Gold deposition was assisted by declining gold, silver, tellurium and sulfur solubility as the fluid cooled. Dissolved sulfate is recorded in pyrite by negative $\delta^{34}S$ (− 10 to − 5‰) at magmatic $\Delta^{33}S$ (0–0.2‰). Oroya ore bodies are subdivided into oxidised pyrite lodes (5 g/t Au) in propylitic GMD and reduced lodes (30–120 g/t Au) characterised by Stage 1 silica–pyrite and siderite–chlorite replacement in ankerite-rich wall rocks. Rapid cooling, an acidic fluid and the retrograde solubility of ankerite facilitated replacement and the deposition of minor arsenopyrite, pyrrhotite, chalcopyrite, sphalerite and gold. Locally, the $H_2S$-rich fluid ($\log f_{S2} = -5.8 \pm 0.5$ bar at 420 °C) was reduced by organic methane. Oroya Stage 2 ore fills crosscutting veins and cements breccia. Quartz, chalcedony, dolomite–ankerite, calcite, V-muscovite, V-chlorite and V-tourmaline form the gangue of pyrite–telluride ± magnetite ore. Altaite–tellurium myrmekites were deposited at ≥ 400 °C as melt droplets together with tellurantimony, altaite, calaverite, montbrayite and petzite. As fluid temperature and tellurium fugacity declined, free gold, krennerite, coloradoite and melonite also crystallised joined by sylvanite and hessite below 350 °C. Finally, trace covellite and digenite precipitated at high fluid sulfidation states.

**Keywords** Kalgoorlie · Golden Mile · Gold · Pyrite · Telluride

Editorial handling: B. Lehmann

**Electronic supplementary material** The online version of this article (https://doi.org/10.1007/s00126-019-00939-8) contains supplementary material, which is available to authorized users.

✉ Andreas G. Mueller
andreasm@iinet.net.au

[1] Centre for Exploration Targeting, School of Earth and Environment, The University of Western Australia, 35 Stirling Highway, Perth, WA 6000, Australia

[2] School of Earth, Atmosphere and Environment, Monash University, Clayton, VIC 3800, Australia

[3] Centre for Microscopy, Characterisation and Analysis (CMCA), The University of Western Australia, 35 Stirling Highway, Perth, WA 6000, Australia

## Introduction

The giant Golden Mile deposit at Kalgoorlie (1767 t Au to December 2018) is located in the Eastern Goldfields Province of the Archean Yilgarn Craton, Western Australia. Production is subdivided into underground (1893–1992, 105.6 Mt at 11.27 g/t Au) and open pit (1984–2018, 302 Mt at 1.91 g/t Au; Electronic supplementary material, ESM App. 1). The deposit and associated porphyry dykes occur in a zone of propylitic alteration more than 4.5 km long and 1 km wide at the surface, controlled by shear zones centred on the D2 Golden Mile strike-slip fault. Genetic models vary from magmatic–hydrothermal (Gustafson and Miller 1937; Mueller et al. 1988; Gauthier et al. 2007) to orogenic–hydrothermal invoking metamorphic fluid generated in the

lower crust during fold-belt evolution (Goldfarb et al. 2005; Groves et al. 2016). Others regard the Golden Mile as a high-level, low-temperature deposit (300–170 °C) similar in style to epithermal Au–Ag deposits (Clout 1989; Shackleton et al. 2003; Voronin et al. 2017).

Structural, petrographic and geochemical studies of ore bodies (lodes) on levels of the Paringa South shaft, mined out during the recent open-pit operation, indicate formation by two hydrothermal systems (Mueller 2017, 2018; this issue). The Fimiston $H_2O$–$CO_2$ fluid was enriched in lithophile elements (Ca, Sr, K, Ba, Rb) and deposited auriferous pyrite ± anhydrite during the sericite–ankerite replacement of propylitic mafic rocks. Oroya-style mineralisation named after the D3 Oroya Shoot (> 62 t Au) overprints Fimiston ore in D2 strike-slip faults such as the Horseshoe No. 4 (> 200 t Au) and Phantom lodes but is the only ore in D3 reverse faults indicating a hiatus in hydrothermal activity. Oroya ore is characterised by an early As–Zn-rich pyrite stage and by a late Sb–Pb-rich sulfide–telluride stage marked by vanadian silicates and oxides. The Oroya $H_2O$–$CO_2$ fluid introduced silica, lithophile elements (Ca, Sr, K, Li, Rb) and, in contrast to the Fimiston fluid, siderophile Fe, Cr, Ni and V (Mueller 2018). The initial $^{87}Sr/^{86}Sr$ isotope ratios of tourmaline and scheelite (Mueller et al. 1991) and the stable isotope ratios of carbonates in the ore bodies and in the late-mineralisation Oroya kersantite dyke implicate the parent plutons of the local monzodiorite–granodiorite dykes as the fluid source (Mueller 2017; Mueller and Muhling 2019).

In this study, the mineralogy of Fimiston- and Oroya-style ore, based on 1360 electron-microprobe analyses, is summarised and interpreted to constrain the *PTX* conditions of gold deposition. The results indicate high fluid temperatures (420–300 °C) and pressure (300 MPa) corresponding to a deep crustal level (10 km) of ore formation and the cooling and reduction of oxidised magmatic fluids during wall-rock interaction. The similarities in magmatic association, alteration and mineralisation style to intrusion-related Cenozoic gold deposits are discussed with emphasis on the Porgera deposit in Papua New Guinea.

## Geologic setting

The Kalgoorlie mining district is located in the Eastern Goldfields Province of the Yilgarn Craton (inset in Fig. 1), a continental-margin orogen characterised by 2.73–2.65 Ga greenstone belts. The stratigraphic, structural and magmatic–metamorphic evolution of the Kalgoorlie terrane is reviewed in Mueller et al. (2016, this issue). The lodes in the Golden Mile are confined to the tholeiitic Paringa Basalt (PB), the

**Fig. 1** Geologic map of the Golden Mile deposit at 300 m above sea level (modified from Mueller 2017) showing the structures according to the time of formation (D1 to D4). The muscovite–paragonite–ankerite zone in Paringa Basalt merges with the paragonite–ankerite–chloritoid zone in Golden Mile Dolerite centred on the D2 Trafalgar Fault (TRF). Minerals: albite (ab), ankerite (ank), calcite (cal), chlorite (chl), dolomite (dol), epidote (ep), muscovite (ms), paragonite (pg). Shafts: Boulder Main (BM), Chaffers (CH), Drysdale (DY), Edwards (ED), Golden Pike (GP), Iron Duke (ID), Lake View Main (LV), North Kalgurli (NK), Paringa South (PS), Perseverance (PV). Drill holes: TRF-1 to TRF-5. Eastern Lodes: B-Lode (B-L), Kelly (KEL), Lake View (LVL), Oroya Hanging Wall (OHW). Western Lodes: Horseshoe No. 3 (H3L), No. 4 (H4L). D2 to D4 faults: Adelaide (ADF), Australia East (AEF), Boulder Lefroy (BLF), Golden Mile (GMF), Golden Pike (GPF). D1 folds: Kalgoorlie Anticline (KLA), Kalgoorlie Syncline (KLS). The coordinates are mine grid. The inset map of Western Australia shows the Eastern Goldfields Province (EGP) in the Archean Yilgarn Craton and the town of Kalgoorlie (K)

600–750-m-thick Golden Mile Dolerite (GMD) and the basal carbonaceous part of the Black Flag greywacke. The differentiated GMD sill at the basalt–greywacke contact is dated at 2685 ± 5 Ma (zircon U–Pb; Tripp 2013) and subdivided into 10 petrographic units. The central Units 6 to 8 are attributed to a second pulse of iron-rich tholeiitic magma (Travis et al. 1971). The succession is folded into the Kalgoorlie Anticline and Syncline (D1) and metamorphosed to the actinolite–albite–zoisite greenschist facies. Igneous textures and pillow structures are well preserved. In Golden Mile Dolerite, augite is pseudomorphed by aggregates of tschermakite, actinolite and accessory chlorite, and calcic plagioclase by albite, zoisite and accessory epidote. Leuxoxene ± ilmenite lamellae outline former Ti-magnetite (Mueller 2017).

The Golden Mile deposit is controlled by the Boulder Lefroy-Golden Mile fault system (D2), which displaces the upright D1 folds 11–12 km in a left-lateral sense (Mueller 2007; Mueller et al. 2016). The steeply dipping shear zones are centred on the Golden Mile Fault and bounded by the Boulder Lefroy Fault in the southwest and by the Trafalgar Fault in the northeast (Fig. 1). Granodiorite porphyry dykes were emplaced into the strike-slip faults at 2676 ± 7 to 2671 ± 10 Ma after D1 metamorphism but prior to propylitic alteration. Barren sericite–ankerite ± chloritoid zones in the Golden Mile Fault, the Trafalgar Fault and at the GMD–PB contact of the Kalgoorlie Anticline (Fig. 1) and subsequent Fimiston ore formation are broadly synchronous with the intrusion of diorite dykes at 2663 ± 11 Ma (Gauthier et al. 2007). The ore bodies are ordered according to their host structure: D2a sinistral strike-slip faults (Fimiston system), D2b sinistral-reverse faults (Australia East system) and D3a reverse faults (Oroya Shoot system). Gold mineralisation took place when periods of D2 strike-slip reactivation alternated with D3a shortening. It ceased before the development of barren D3b thrusts (Mueller 2017).

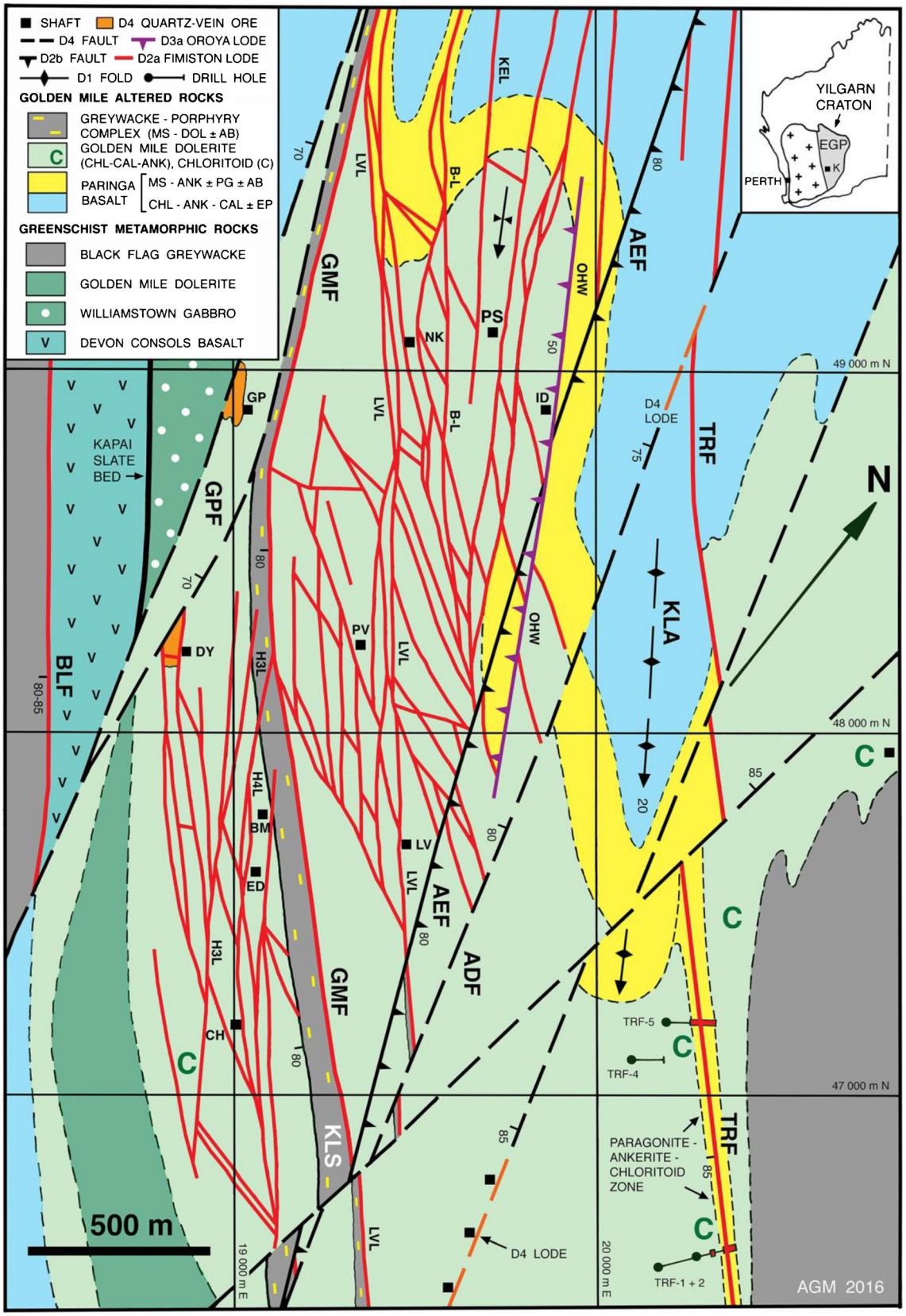
SHAFT
D4 QUARTZ-VEIN ORE
D4 FAULT
D3a OROYA LODE
D2b FAULT
D2a FIMISTON LODE
D1 FOLD
DRILL HOLE
GOLDEN MILE ALTERED ROCKS
GREYWACKE - PORPHYRY COMPLEX (MS - DOL ± AB)
GOLDEN MILE DOLERITE (CHL-CAL-ANK), CHLORITOID (C)
PARINGA BASALT
MS - ANK ± PG ± AB
CHL - ANK - CAL ± EP
GREENSCHIST METAMORPHIC ROCKS
BLACK FLAG GREYWACKE
GOLDEN MILE DOLERITE
WILLIAMSTOWN GABBRO
DEVON CONSOLS BASALT
YILGARN CRATON
EGP
K
PERTH
KAPAI SLATE BED
GMF
GPF
BLF
KEL
LVL
B-L
OHW
AEF
ADF
TRF
KLA
KLS
H3L
H4L
D4 LODE
PARAGONITE - ANKERITE - CHLORITOID ZONE
GP
NK
PS
ID
DY
PV
LV
BM
ED
CH
TRF-5
TRF-4
TRF-1 + 2
49 000 m N
48 000 m N
47 000 m N
19 000 m E
20 000 m E
500 m
AGM 2016
N

### Pre-sulfide hydrothermal alteration

In Golden Mile Dolerite, the ore bodies overprint propylitic assemblages. Metamorphic amphibole in augite sites is replaced by chlorite and minor Fe-calcite, and zoisite in plagioclase sites by calcite, albite and epidote again preserving the igneous texture. Metamorphic leucoxene is altered to rutile. Remnant primary Ti-magnetite is confined to GMD Units 6 and 7 (Travis et al. 1971; Bartram and McCall 1971). In Paringa Basalt, the ore bodies overprint sericite–ankerite assemblages in a contact zone about 150 m thick (Fig. 1). In this zone, part of the albite is replaced by microcrystalline quartz, muscovite and paragonite. Micron-sized rutile is evenly, whereas chlorite and magnetite are locally disseminated.

### Ore bodies in the Paringa South mine

The Paringa South mine (Fig. 1) produced 4.0 Mt at 19.4 g/t Au (1893–1967) and 0.626 Mt at 4.36 g/t Au (1983–1987). The locations, structural setting, petrography and geochemistry of the ore bodies sampled are described in Mueller (1990, 2017, 2018). Gold mineralisation is subdivided into: (1) early Fimiston refractory pyrite ore; (2) Oroya Stage 1 ore characterised by pyrite + arsenopyrite ± pyrrhotite; and (3) Oroya Stage 2 ore characterised by vanadian muscovite, free native gold and tellurides. Fimiston ore is represented by the D2a Kelly Lode and B-Lode and by parts of the D2b Blatchford shear zone. Oroya-style ore is represented by the by the D2b Blatchford shear zone and vein and by the D3a Oroya Hanging Wall (OHW) Lode. The mineralogy of the Paringa South ore bodies is compared to data from the Horseshoe No. 4 Lode and from the high-grade Phantom Lode, both located close to the central Golden Mile Fault (ESM Fig. 1). The occurrence of enargite–famatinite and realgar in the No. 4 Lode and of copper sulfides in both ore bodies (see summary in ESM Fig. 1) constrains late-stage ore formation.

## Analytical methods and terminology

Gangue and ore minerals in samples from the Paringa South lodes and from the D3a Flat Lode on the North Kalgurli shaft 13 level were examined in transmitted and reflected polarised light in 70 covered or polished thin sections and in 23 polished mounts. Selected sections and mounts were analysed by the senior author in the JEOL JXA-8530F field emission electron microprobe at the Centre for Microscopy, Characterization and Analysis (CMCA), the University of Western Australia. The averages and standard deviations of 768 wavelength dispersive (WDS) analyses of silicates, carbonates, phosphates and oxides and of 580 WDS analyses of sulfides, tellurides and native gold are listed in the Electronic supplementary material (ESM tables and appendices). Tiny inclusions (≤ 1 μm) of native gold and telluride in pyrite were imaged in backscattered electron (BSE) mode in a Verios 460 field emission scanning electron microscope (SEM). Energy-dispersive (EDS) analyses were carried out using the Oxford Instruments SDD detector and the AZtec database of standards. The inclusions were identified by molar ratio after eliminating the signals of the host pyrite. Instrument settings, calibration standards, detection limits and methods to estimate ferric iron are described in ESM Appendix 1.

Chlorite thermometry (error ± 50 °C) is based on the calibrations of Cathelineau (1988) and Lanari et al. (2014). The WDS microanalyses were recast using the software AX of Holland and Powell (2000), which allocates ferric iron by setting the total number of cations to 10 for 14 oxygens (Laird 1988). The results suggest that the iron in all chlorites is ferrous. The temperatures based on Lanari et al. (2014) are calculated at 200 and 300 MPa, the median isochore pressures of fluid inclusions in D3a reverse and D2a strike-slip faults, respectively (Ho et al. 1990). The chlorite data are complemented by arsenopyrite thermometry (details in ESM App. 1) using the calibration of Kretschmar and Scott (1976). The thermodynamic modelling of mineral equilibria at 300 MPa and elevated temperature (> 250 °C) was carried out using the software HCh (Shvarov 2008; Xing et al. 2019) and CHNOSZ (Dick 2008) and the thermodynamic datasets Unitherm (Shvarov 2008) and SUPCRTBL (Zimmer et al. 2016).

The term "silica" is applied to dense chert-like quartz, and "chalcedony" to microcrystalline quartz marked by local pores and fibrous crystals (Deer et al. 1992). The term "sericite" denotes white mica, "phengite" muscovite with $^{IV}Si > 3.1$ and "paragonite" white mica with a ratio $K/(K + Na) < 0.15$ (International Mineralogical Association, IMA 1999; Fleet 2003). Carbonates of the dolomite–ankerite and magnesite–siderite solid-solution series are subdivided by their Fe/(Mg + Fe) ratio: dolomite < 0.2, ankerite 0.2 to 0.7 and siderite > 0.7 (Chang et al. 1998). Minerals in equilibrium contact are joined by hyphens or plus signs.

## Mineralogy of Fimiston ore

The B-Lode on the Paringa South shaft 6 level consists of fault-fill veins surrounded by red albite–phengite–ankerite selvages grading into outer chloritic ankerite replacement in GMD Unit 4. Pyrite in the vein selvages (10 vol%) is in contact with magnetite and specular hematite (Mueller 2018). The Kelly Lode on 4 level was mapped at the southeast termination of this ore body. The array of fault-fill veins narrows and

the pyrite-rich inner vein selvages decrease in abundance and width. They enclose remnant domains of propylitic GMD Unit 2 exposed in chlorite–calcite–albite facies below the lode. Magnetite and hematite are absent. The Blatchford Lode on 11 level crosscuts sericite–ankerite-altered Paringa Basalt. Fimiston ore in the S-C mylonite of the main shear zone is exposed 20 m northwest of the telluride extension vein mapped (Mueller 2018).

## Quartz, albite and tourmaline

In Golden Mile Dolerite, the brittle veins are filled with granular quartz, albite, Fe-calcite and dolomite–ankerite (Fig. 2a). Fault-fill veins in major movement planes display brecciation and re-cementation (Fig. 6 in Mueller 2018). Quartz grain boundaries are sutured and partly lined with microcrystalline seams. In places, strained quartz crystals indicate extensional fibrous growth (Fig. 2b). Albite is marked by strained twin lamellae (Fig. 2c). Quartz and albite are pure except for trace iron (ESM App. 2).

Fine-grained quartz, albite and dolomite–ankerite are also major constituents in the vein selvages together with white mica and pyrite (Fig. 2a). The amount of albite decreases away from the vein. Chlorite (0.5 vol%) and tourmaline (1%) occur in contact with pyrite (Fig. 2d, e). The tourmaline classifies as dravite characterised by fluorine

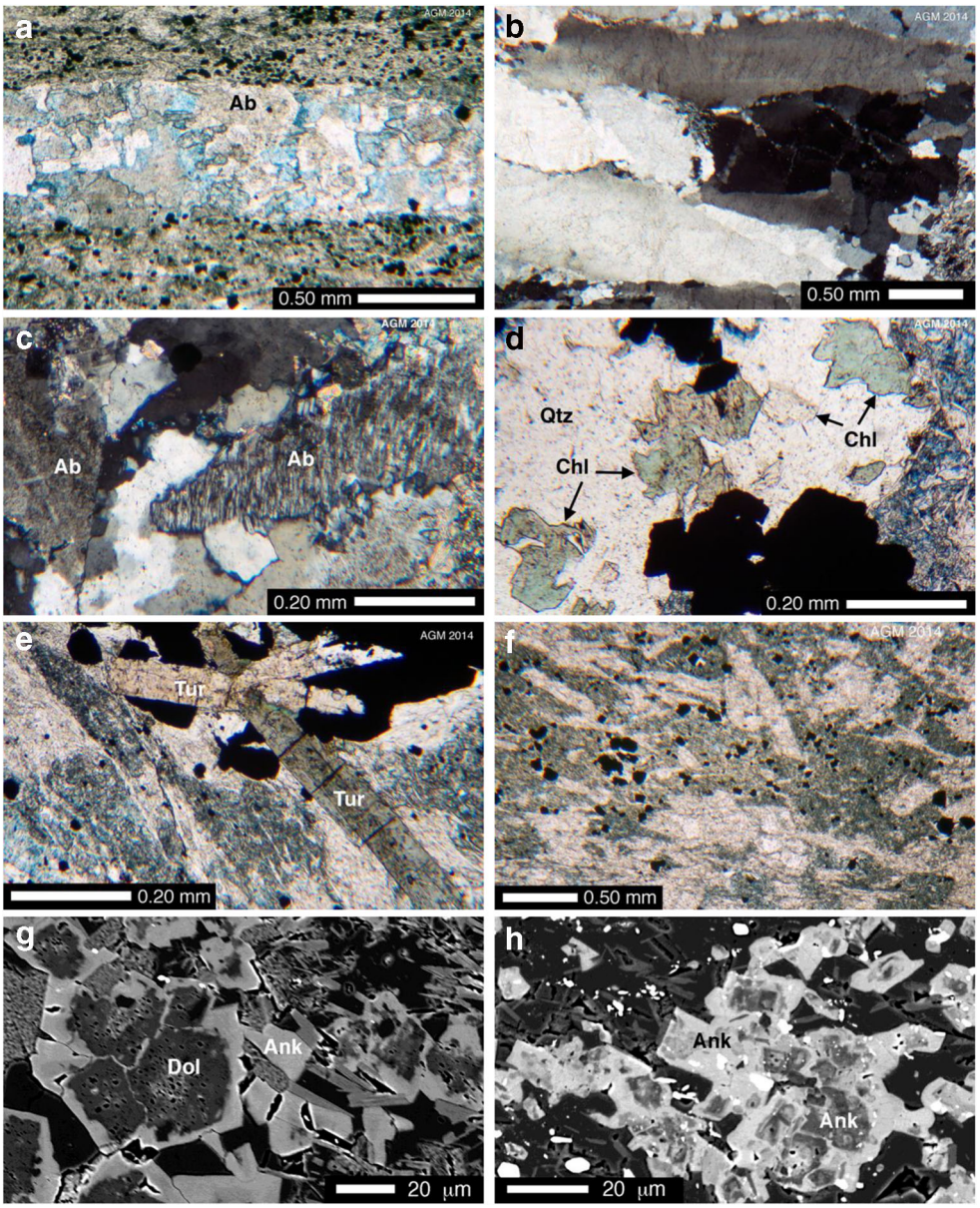


**Fig. 2** Gangue minerals in Fimiston ore from the Kelly Lode (**a**–**g**) in propylitic Golden Mile Dolerite and from the Blatchford shear zone (**h**) in sericite–ankerite-altered Paringa Basalt, Paringa South shaft 4 and 11 levels, photomicrographs in plane and crossed polarised light (PPL, XPL), and backscattered electron (BSE) images. **a** Fault-fill vein composed of quartz, zoned dolomite–ankerite (not stained to light blue), albite (Ab) and Fe–calcite (stained dark blue). Opaque pyrite is abundant in the wall rock; sample KL-5, PPL. **b** Fault-fill vein, strained columnar quartz crystals rim a wall-rock fragment, KL-8a, XPL. **c** Fault-fill vein, albite (Ab) marked by strained twins in contact with quartz and dolomite–ankerite, KL-11, XPL. **d** Vein replacement selvage, quartz (Qtz) and chlorite (Chl) in contact with opaque pyrite, ankerite (stained blue) and muscovite, KL-20, PPL. **e** Vein selvage, pleochroic tourmaline (Tur) in contact with opaque pyrite in ankerite (stained blue), muscovite and quartz, KL-22b, PPL. **f** Outer zone in GMD Unit 2, igneous texture: augite sites (dark) are replaced by opaque pyrite + ankerite, and plagioclase laths by muscovite + quartz, KL-5, PPL. **g** Vein selvage, poikilitic dolomite (Dol) zoned to ankerite rims (Ank) in muscovite, quartz and albite, KL-11, BSE. **h** S-C mylonite, ankerite (Ank) zoned to Fe-rich rims in quartz (dark grey), muscovite (grey) and pyrite (white), BLF-12, BSE

below detection, a low cation ratio Ca/(Ca + Na), low vacancy in the X-site (0.265), an average Fe/(Mg + Fe) ratio of 0.45 ± 0.03 (1$\sigma$) and ≤ 0.56 wt% $V_2O_3$ (ESM App. 2).

In the Kelly and B-Lode, an intermediate zone of feldspar-destructive hydrolytic alteration separates the albite-stable vein selvages from outer propylitic GMD, where albite is part of the pre-sulfide chlorite–calcite assemblage (ESM App. 2). In the hydrolytic zone, 0.5–1 m wide in the B-Lode (Fig. 4 in Mueller 2018), most albite is replaced by microcrystalline phengite + quartz, whereas the propylitic chlorite is replaced by ankerite, minor pyrite ± magnetite and newly formed chlorite (Fig. 2f).

Albite was not detected in the S-C mylonite of the Blatchford shear zone, which overprints pre-sulfide sericite–ankerite alteration in Paringa Basalt. Pinch-and-swell granular quartz–ankerite veins alternate with quartz–sericite, ankerite and pyrite–tourmaline seams (Fig. 10 in Mueller 2018).

## Carbonate and apatite

Carbonates of the dolomite–ankerite series are major phases in the B-Lode and Kelly Lode and in the No. 4 Lode southwest of the Golden Mile Fault (Golding and Wilson 1983). The abundance of ankerite, phengite and pyrite in the outer hydrolytic zone defines the boundary of "lode alteration" to the older propylitic chlorite–calcite zone. Calcite (1–20 vol%) is present in the fault-fill veins, and fluor-apatite (0.5%) in vein selvages of the B-Lode (ESM App. 2). Many carbonate grains are zoned. In Fimiston ore lacking iron oxides, microprobe analyses and BSE images (Fig. 2g, h) show an increase in the cation ratio Fe/(Mg + Fe) with time, distinct in both the Blatchford (core 0.35, rim 0.57) and Kelly lodes (core 0.14, rim 0.29). The opposite trend is observed in the B-Lode, where ankerite crystallised together with magnetite and hematite (core 0.43; rim 0.36; ESM App. 3).

## White mica and chlorite

Dioctahedral K-Na white mica (Ca < 0.008) varies in composition between alteration styles in the Paringa South mine (ESM App. 4). The outer part of the pre-sulfide contact zone in GMD Unit 1 is characterised by mixed-layer paragonite–muscovite ± phengite (Fig. 3a), whereas all ore bodies are characterised by muscovite and phengite (Fig. 3b). The ratio K/(K + Na) = 0.50 divides barren from mineralised alteration. The mica in GMD-hosted lodes, where albite is stable in the vein selvages, classifies mostly as K-rich phengite ($^{IV}$Si > 3.1) charge-balanced by a component of ferro-alumino celadonite (Mg + $Fe^{2+}$) at low contents of octahedral vanadium ($^{VI}$V < 0.015; Fig. 3c). The allocation of ferric iron, based on cation stoichiometry (ESM App. 1), is high in B-Lode mica ($Fe_2O_3$ = 1.7–1.8 wt%) and lower in Kelly Lode mica (0.34%; ESM App. 4) correlating with the presence and absence of iron oxides, respectively. The white mica in Fimiston ore of the Blatchford shear zone, where albite is absent, is muscovite of distinctly lower K/(K + Na) ratio than in the GMD-hosted lodes (Fig. 3b). Its contents of octahedral Mg, Fe and V are low (Fig. 3c), and ferric iron was not allocated (ESM App. 4).

Chlorite is rare in the veins and vein selvages of the GMD-hosted lodes (Fig. 2d) and absent in Fimiston ore of the Blatchford shear zone. It is the main mineral in propylitic GMD Unit 2 below the Kelly Lode and minor (5 vol%) in the outer hydrolitic zone of the B-Lode, where it forms part of the ankerite–magnetite–pyrite replacement in augite sites of GMD Unit 4 (Mueller 2018). The chlorite analyses from these two localities (ESM App. 5) define a linear trend of increasing Fe/(Mg + Fe) and tetrahedral Al (Fig. 3d) determined by host-rock composition and by $^{IV}$Al-temperature (Cathelineau 1988).

## Rutile, magnetite and hematite

In propylitic Golden Mile Dolerite and in GMD-hosted Fimiston Lodes, rutile (1–3 vol%) replaces the ilmenite lamellae and rims of former Ti-magnetite (Fig. 4a). The rutile contains minor $V_2O_3$ (≤ 0.32 wt%) and FeO (ESM App. 6). In sericite–ankerite-altered Paringa Basalt, rutile forms anhedral or needle-shaped grains (2–15 μm), which line the foliation planes of the Blatchford shear zone (Mueller 2018).

Hydrothermal magnetite and hematite are present in the B-Lode. Disseminated sub- to euhedral magnetite (3 vol%) is partly replaced by hematite, in particular in the pyrite-rich selvages of the fault-fill veins. Early magnetite–pyrite gives way to late hematite–pyrite although all three minerals are locally in equilibrium contact (Fig. 4b). The $V_2O_3$ content of magnetite decreases away from the veins (0.34 to 0.12 wt%). Specular hematite contains $V_2O_3$ (0.51 wt%) and ilmenite in solid solution (8 mol%; ESM App. 6).

## Fimiston sulfides and tellurides

Subhedral pyrite (5 μm to 1 mm) is the main sulfide in Fimiston ore (average 10 vol%). In the GMD-hosted lodes, most is disseminated in the replacement selvages adjacent to fault-fill veins (Fig. 2a). Arsenic substitutes for sulfur, and cobalt and nickel for iron in pyrite (ESM App. 7). Arsenic is below detection in Kelly Lode pyrite, but cobalt and nickel are enriched in the core of a few grains (≤ 0.71 wt% Co; ≤ 0.43% Ni). In the B-Lode, arsenic and cobalt increase laterally from the inner (< 0.05% As, 0.24% Co) to the outer replacement zone (≤ 0.78% As, 2.05% Co), where arsenical pyrite is in contact with tennantite and cobaltite

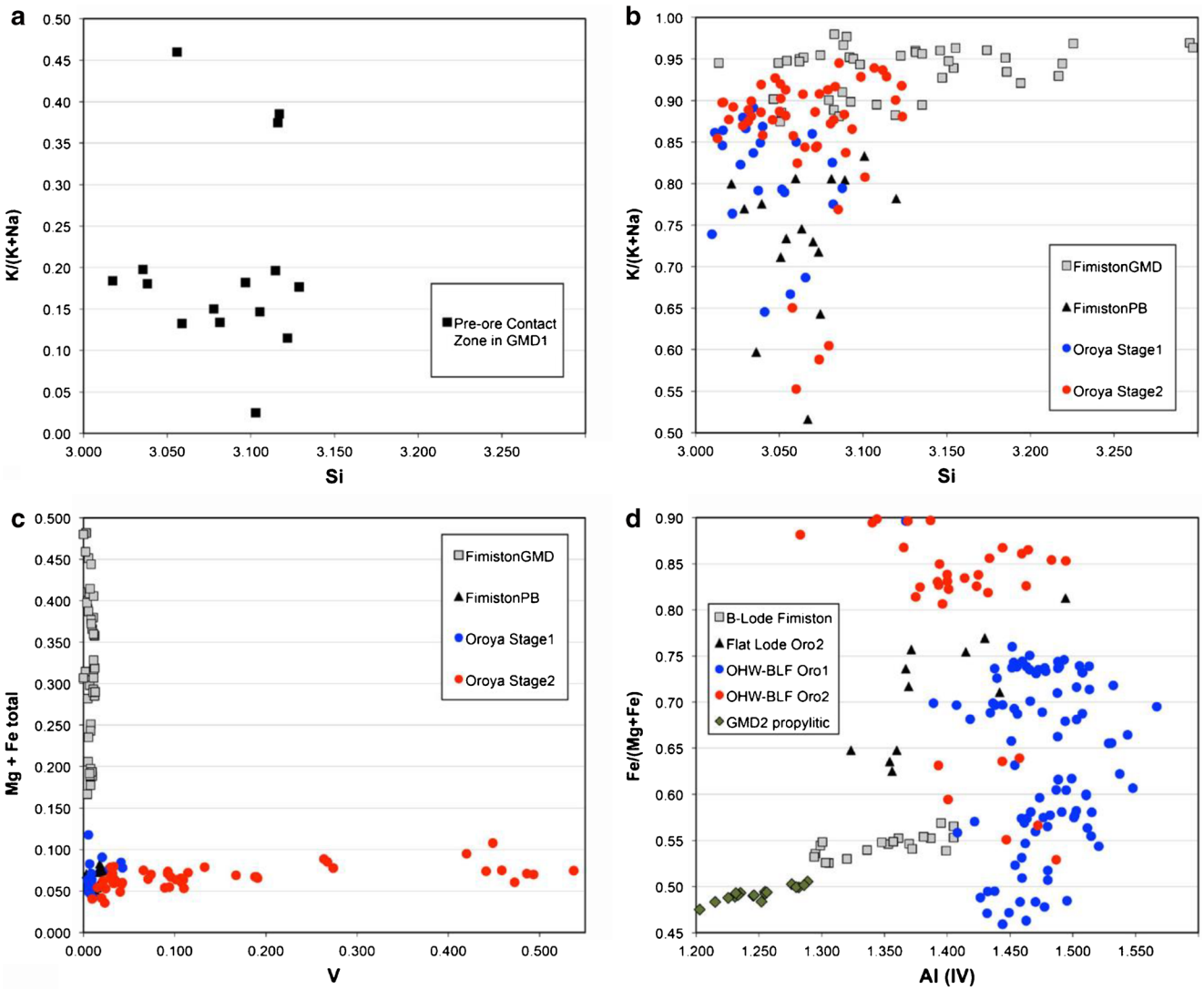


**Fig. 3** White mica and chlorite cation diagrams illustrating compositions in propylitic Golden Mile Dolerite (GMD), the pre-sulfide sericite-ankerite zone in Paringa Basalt (PB) at the GMD contact, Fimiston ore and Oroya ore, Paringa South shaft 4 to 11 levels and North Kalgurli shaft 13 level. **(a)** Mica K/(K + Na) versus tetrahedral Si, pre-sulfide contact zone in GMD Unit 1, crosscut on 7 level. **(b)** Mica K/(K + Na) versus tetrahedral Si, Fimiston ore in GMD (B-Lode, Kelly Lode), Fimiston ore in PB (Blatchford shear zone), and Oroya Stage 1 and Stage 2 ore in PB (OHW Lode, Blatchford shear zone and vein). **(c)** Mica octahedral Mg + $Fe_{total}$ (Tschermak substitution) versus octahedral V in Fimiston and Oroya ore, lodes as in (b) above. **(d)** Chlorite Fe/(Fe + Mg) versus tetrahedral Al in propylitic GMD Unit 2 below the Kelly Lode, in the outer B-Lode (Fimiston), in the OHW Lode and Blatchford shear zone (Oroya Stage 1), and in the OHW Lode, Blatchford vein and Flat Lode (Oroya Stage 2)

(Fig. 4c; ESM Table 1). In the PB-hosted Blatchford shear zone, Fimiston-style pyrite forms seams along the S-C foliation (Fig. 4d). This pyrite is zoned from poikilitic arsenical cores (≤ 3.02% As) to solid As-poor rims (≤ 0.40% As). Cobalt is low (≤ 0.21% Co), and nickel below detection.

Native gold (1–40 μm) enclosed in or interstitial to pyrite has a fineness of 920 (13.8 at% Ag; normalised to 100% Au + Ag + Hg + Sb + Bi). Trace Hg, Bi and Te were detected in some grains (ESM Table 1). Most gold in Fimiston pyrite, however, occurs in submicron native grains (Fig. 4e) or in telluride inclusions (Fig. 4f). Petzite, coloradoite and melonite were identified in Kelly Lode pyrite, and petzite, hessite and coloradoite in B-Lode pyrite (ESM App. 8). The low Au/Ag ratio of B-Lode and Kelly Lode ore (0.43–0.72) suggests a predominance of petzite inclusions, whereas the ratio of bulk Fimiston ore (2.06) indicates that native gold and calaverite are most abundant (Mueller 2018). Chalcopyrite (0.1–0.5 vol%; Fig. 4a, c) is present in all Fimiston ore, whereas sphalerite is absent.

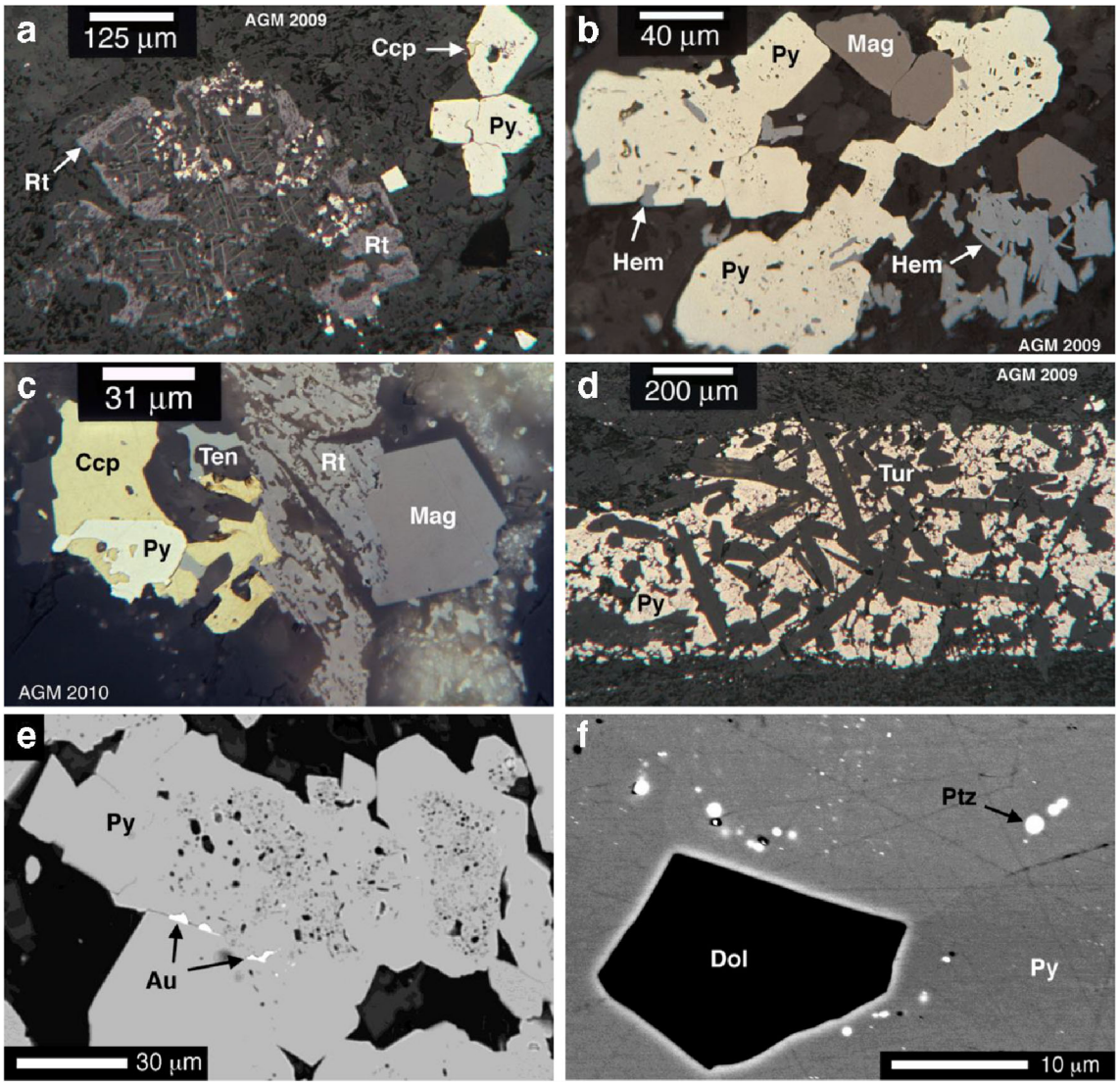


**Fig. 4** Oxides, sulfides, tellurides and gold in Fimiston ore from the Kelly Lode (**a**, **f**) and B-Lode (**b**, **c**) in propylitic Golden Mile Dolerite (GMD), and from the Blatchford shear zone (**d**, **e**) in sericite–ankerite-altered Paringa Basalt (PB), Paringa South shaft 4 to 11 levels, photomicrographs in plane polarised light reflected in air (PPL) and backscattered electron (BSE) images. **a** Inner zone in GMD: rutile (Rt) after ilmenite rims rutile trellis after Ti-magnetite, pyrite (Py) in contact with chalcopyrite (Ccp), sample KL-11, PPL. **b** Inner zone in GMD: equilibrium assemblage, pyrite (Py) in contact with euhedral magnetite (Mag) and specular hematite (Hem), PAR-7rd, PPL. **c** Outer zone in GMD: pyrite (Py), chalcopyrite (Ccp) and tennantite (Ten) in contact with rutile (Rt) partly replaced by magnetite (Mag), PAR-7gn, PPL. **d** S-C mylonite in PB: foliation-parallel band of arsenical pyrite (Py) and tourmaline (Tur), BLF-12, PPL. **e** S-C mylonite in PB: native gold (Au) at grain boundaries and enclosed in pyrite (Py) zoned from poikilitic As-rich cores to solid As-poor rims, BLF-12, BSE. **f** Inner zone in GMD: pyrite (Py) encloses dolomite (Dol) and globular grains of petzite (Ptz) identified by EDS analysis (ESM App. 8), KL-11, BSE

## Mineralogy of Oroya ore

The Blatchford and OHW lodes replace barren sericite–ankerite-altered Paringa Basalt. In the D2b Blatchford Lode on the Paringa South shaft 11 level, Oroya-style mineralisation overprints Fimiston ore in the rise to the 1109 sublevel, where an extension vein branches off the main shear zone (Fig. 9 in Mueller 2018). Oroya Stage 1 pyrite–pyrrhotite ± arsenopyrite ore is present in the shear zone and in the outer part of the zoned vein, whereas Stage 2 telluride ore fills the central vein (120 g/t Au). The D3a Oroya Hanging Wall (OHW) Lode replaces altered basalt below the GMD contact at the SW-limb of the Kalgoorlie Anticline. On the Paringa South shaft 7 level, the lode is composed of mylonite and breccia containing Stage 1 pyrite–arsenopyrite ± pyrrhotite and Stage 2 telluride ore (48 g/t Au).

In contrast, the Flat Lode on the North Kalgurli shaft 13 level replaces propylitic GMD Unit 5 and occurs in a D3a reverse fault offsetting the steeply dipping D2a Lake View Lode. Massive Stage 1 siderite ± silica–chlorite fault fill is brecciated and cemented by Stage 2 (?) ankerite, minor siderite, chlorite and

quartz. Early magnetite + pyrite is overprinted by hematite + pyrite. High-grade Au–Te–V ore is absent, and the refractory hematite–pyrite ore (5 g/t Au) is tentatively assigned to Stage 2.

## Chalcedony, quartz and tourmaline

One of the characteristic features of Oroya ore is the abundance of Stage 1 chert-like quartz (silica) coloured grey by disseminated pyrite (Fig. 5a). Local pores and fibrous crystals in the outer zone of the Blatchford extension vein (Fig. 5b) suggest that the silica represents partly recrystallised chalcedony. In the shear zones, strain caused recrystallisation to a granular mosaic (Fig. 5c), local brecciation and cementation by siderite, chlorite and pyrite (Fig. 5d). Stage 2 comb-textured quartz and calcite crystals in the centre of the Blatchford extension vein are cemented by granular silica and minor carbonate. The quartz is pure except for trace FeO (0.2–0.5 wt%; ESM App. 2). Albite was not detected in

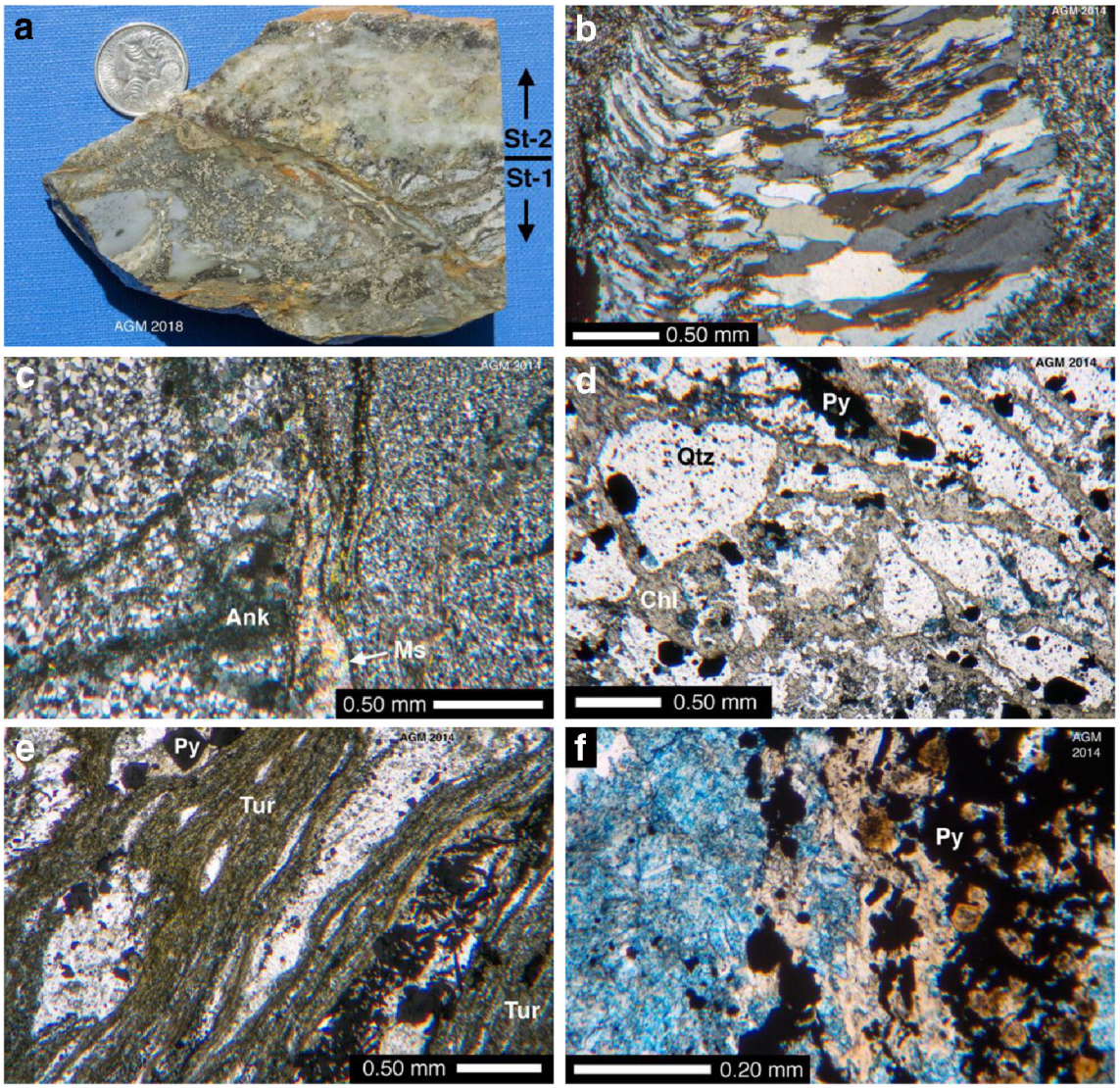


**Fig. 5** Chalcedony, quartz and tourmaline in Oroya Stage 1 and Stage 2 ore from the Blatchford extension vein (**a**, **b**) and the OHW Lode (**c**–**f**) in sericite–ankerite-altered Paringa Basalt, Paringa South shaft 7 and 11 levels, photomicrographs in plane and crossed polarised light (PPL, XPL), and photograph of vein fill. **a** Vein: Oroya Stage 1 (St-1) chalcedony margin, minor pyrite (15 vol%), chalcopyrite (2%), arsenopyrite (1–2%) and pyrrhotite (1%). Oroya Stage 2 (St-2) central vein, grey quartz crystals and interstitial chalcedony + dolomite + calcite (40%), V-muscovite (5%), pyrite (7%), chalcopyrite (1%), sphalerite (0.5%), tellurides (0.1–0.5%) and native gold (0.1%), sample BLF-11, the coin is 19 mm across. **b** Vein: Stage 1 chalcedony composed of fibrous and granular quartz, interstitial muscovite, BLF-2d, XPL. **c** Fault: Recrystallised chert-like quartz, ankerite-veined (Ank) Stage 2 clear quartz (left) and Stage 1 dark quartz (right) enclosing micron-sized pyrite (opaque); muscovite (Ms) lines the contact, OHW-8c, XPL. **d** Fault: Stage 1 breccia, fragments of chert-like quartz (Qtz) cemented by chlorite (Chl), siderite, pyrite (Py), and trace ankerite (blue), OHW-10b, PPL. **e** Fault: Stage 1 mylonite, lenses of chert-like quartz (white) containing opaque pyrite (Py), arsenopyrite needles and accessory chlorite are enclosed in fibrous tourmaline (Tur), OHW-22, PPL. **f** Fault: Stage 2 pyrite (Py), red-brown V-tourmaline and pink Fe–V chlorite in contact with ankerite (stained blue), OHW-8c, PPL

the two basalt-hosted lodes but is a minor phase in veins of the Flat Lode (Mueller 2018).

Blue-grey or red-brown tourmaline is accessory (0.5–2 vol%) in Stage 1 ore of the Blatchford and Flat Lodes but is abundant (up to 20%) in the siliceous mylonite of the OHW Lode (Fig. 5e). The Stage 1 tourmaline classifies as schorl characterised by fluorine below detection, moderate vacancy in the X-site (0.309), an Fe/(Mg + Fe) ratio of 0.57 ± 0.05 (1$\sigma$), a low cation ratio Ca/(Ca + Na) and ≤ 0.54 wt% $V_2O_3$ (ESM App. 2). The Stage 2 tourmaline in the OHW Lode (Fig. 5f) classifies mostly as schorl given an Fe/(Mg + Fe) ratio of 0.53 ± 0.04 (1$\sigma$), but has higher fluorine (0.09 ± 0.07 wt%), more vacancies in the X-site (0.338) and higher vanadium contents (up to 1.16 wt% $V_2O_3$; ESM App. 2). Stage 2 tourmaline in the telluride-rich Oroya Shoot is bright ruby red (6.03–14.65% $V_2O_3$; Mueller and Muhling 2019).

## Carbonates and apatite

Carbonates of the dolomite–ankerite series are major phases in both Oroya Stage 1 and Stage 2 gold ore, whereas siderite is characteristic of Stage 1. Calcite is abundant in Stage 2 fill of the Blatchford vein, and fluor-apatite (0.5 vol%) was detected in Stage 2 ore of the OHW Lode (ESM App. 2). Carbonate core–rim compositions (ESM App. 3) are quoted below as Fe/(Mg + Fe) cation ratios. In the oxidised Flat Lode, microcrystalline siderite in Stage 1 fault-fill is zoned from Fe-rich cores (0.81) to Mg-rich rims (0.60; Fig. 6a). The siderite is brecciated and locally replaced by chlorite, silica and pyrite-iron oxide assemblages (Fig. 6b). In the breccia cement, ankerite (0.49) is dominant.

In Stage 1 ore of the OHW Lode, siderite predominates over ankerite. Most siderite grains are weakly zoned (Fig. 6c). The ankerite is zoned from Mg-rich cores (0.37) to Fe-rich rims (0.48). In Stage 2 ore, siderite is accessory and ankerite predominant. Many grains are zoned from dolomite cores (0.17) to ankerite rims (0.40; Fig. 6d). In Stage 1 ore of the Blatchford shear zone, foliation-parallel veins are filled with granular quartz, Fe-calcite and ankerite. Fe-calcite partly replaces the fragments in fault breccia. Siderite and ankerite predominate in the Stage 1 silica replacement of both shear zone and vein. Most ankerite is zoned to Fe-rich rims. In Stage 2 ore of the vein, siderite is rare and calcite is most abundant (Fig. 6e). Calcite is zoned to Fe-rich rims, and dolomite (0.03) to ankerite rims (0.45; Fig. 6f).

## White mica and chlorite

Dioctahedral K-Na white mica (Ca < 0.010) is minor in both Oroya Stage 1 and Stage 2 ore (5–10 vol%), less abundant than chlorite in the OHW Lode and about equally abundant in the Blatchford Lode. All Stage 1 and the majority of Stage 2 micas classify as muscovite ($^{IV}$Si < 3.1; Fig. 3b) due to low levels of the Tschermak substitution [$^{IV}$Si $^{VI}$(Mg,Fe) = $^{IV}$Al $^{VI}$Al]. In the absence of albite, the mica K/(K + Na) ratios range from 0.55 to 0.95 (Fig. 3b). Seven analyses plot below the muscovite limit of 0.7 (IMA 1999) suggesting paragonite interlayers. On average, the Oroya muscovite lacks ferric iron and is more Na-rich than phengite in the GMD-hosted Fimiston Lodes (ESM App. 4). Compositional trends include the enrichment in potassium and vanadium from Stage 1 to Stage 2 (Fig. 3b, c). Trivalent vanadium substitutes for $Al^{3+}$ (Fleet 2003) and fills up to one quarter of the octahedral sites (Fig. 3c), below the ideal composition of roscoelite ($KV_2AlSi_3O_{10}[OH]_2$; IMA 1999).

Chlorite is in contact with white mica and shares the trend in vanadium enrichment from Stage 1 to Stage 2. The pleochroism varies from pale yellow to brown-grey (Fig. 5d) or dark green (Fig. 6b) in Stage 1, and to pink (Fig. 5f) or orange-red in Stage 2. In the OHW Lode, chlorite forms stylolite seams in recrystallised silica. Relative to Fimiston B-Lode chlorites, the Stage 2 OHW and Blatchford chlorites are mostly higher in $^{IV}$Al, whereas the Stage 1 chlorites are consistently higher (Fig. 3d) indicating high temperatures of crystallisation. The Flat Lode chlorites overlap in $^{IV}$Al with B-Lode chlorites. In contrast, the Fe/(Mg + Fe) ratios of all Oroya chlorites vary widely illustrating the lack of temperature dependence and host-rock control (Fig. 3d). On average, $^{IV}$Al in chlorite decreases from Stage 1 to Stage 2 in both the OHW and Blatchford Lode, whereas the Fe/(Mg + Fe) ratio increases (ESM App. 5).

## Rutile, magnetite and hematite

Rutile is sparse in the extensional sections of D3a reverse faults (Flat Lode, OHW Lode) and in the Blatchford vein, where mineral fill resulted in the dilution of $TiO_2$ inherited from the host rocks (Mueller 2018). Rutile trellis after Ti-magnetite is confined to thin muscovite–chlorite schist replacing GMD Unit 1 at the hanging wall contact of the OHW Lode. Micron-sized grains and needles line S-C foliation surfaces in basalt-hosted mylonite and cluster in the chalcedony zone of the Blatchford vein.

Magnetite– and hematite–pyrite aggregates occur in the Flat Lode, where they partly replace siderite fragments (Fig. 6b) adjacent to ankerite–chlorite–quartz cement. The magnetite (Fig. 7a) contains minor vanadium (0.21 wt% $V_2O_3$) and is locally zoned to low-V rims. Hematite replacing magnetite is enriched in vanadium

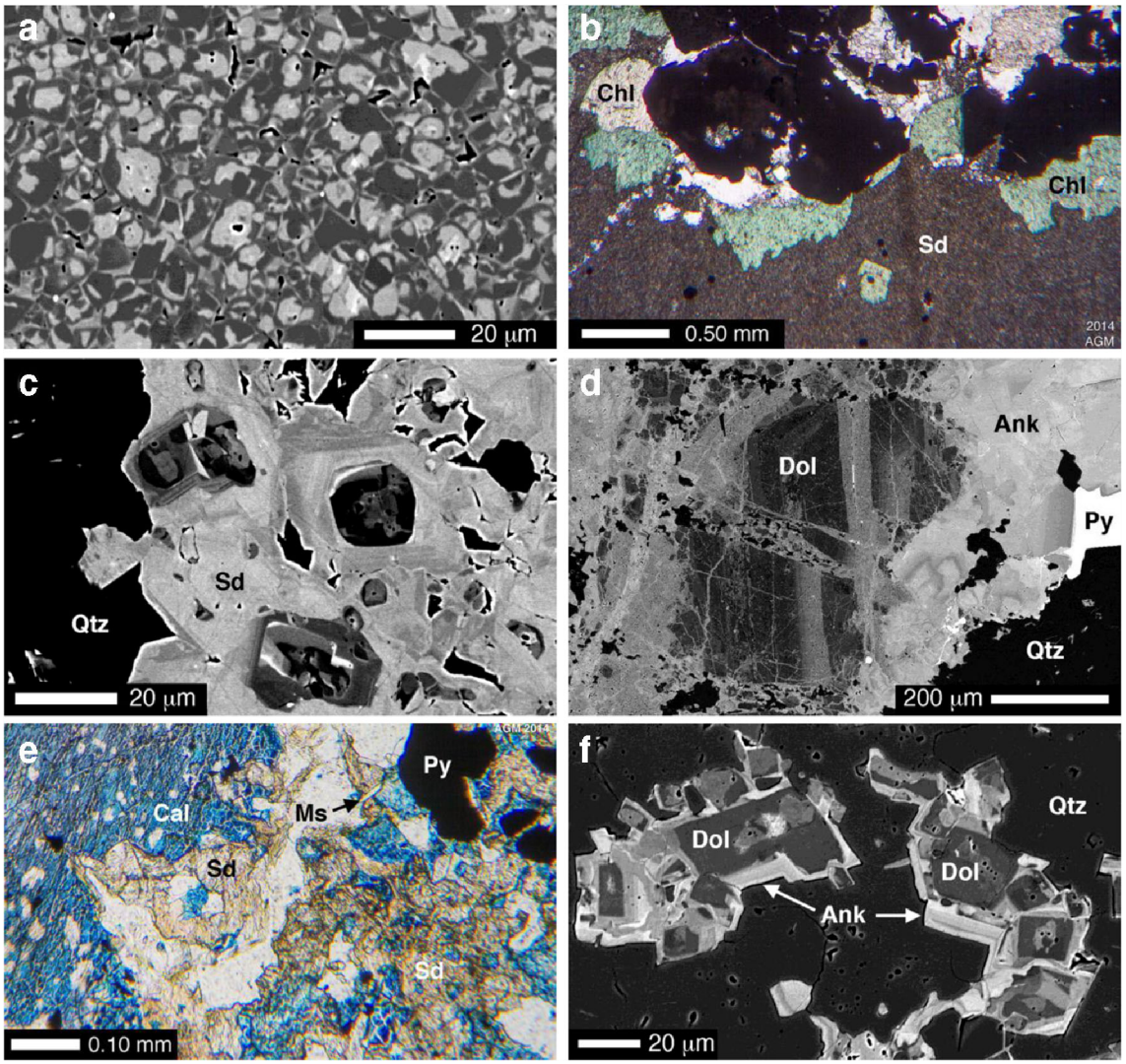


**Fig. 6** Carbonates in Oroya Stage 1 and Stage 2 ore from the Flat Lode (**a**, **b**) in propylitic Golden Mile Dolerite, North Kalgurli shaft 13 level, and the OHW Lode (**c**, **d**) and Blatchford vein (**e**, **f**) in sericite–ankerite-altered Paringa Basalt, Paringa South shaft 7 and 11 levels, photomicrographs in plane and crossed polarised light (PPL, XPL) and backscattered electron (BSE) images. **a** Stage 1 fault-fill: siderite zoned from Fe-rich cores (light grey) to Mg-rich rims (dark grey), sample FLO-2, BSE. **b** Stage 1 siderite (Sd) partly replaced by Stage 2 (?) opaque iron oxides, pyrite, chlorite (Chl) and interstitial quartz + ankerite (white-grey), FLO-2, PPL. **c** Stage 1 chert-like quartz (Qtz) in contact with siderite (Sd) zoned from Mg-rich cores (dark) to wide Fe-rich rims (light), OHW-11a, BSE. **d** Stage 2 fractured dolomite (Dol) zoned to ankerite rims (Ank) in contact with chert-like quartz (Qtz) and pyrite (Py), OHW-9c, BSE. **e** Stage 1–2 transition zone, ferroan calcite (Cal, stained blue), siderite (Sd, not stained), chert-like quartz (white), muscovite (Ms) and opaque pyrite (Py), BLF-1, PPL. **f** Stage 2 dolomite (Dol) zoned to ankerite rims (Ank) in quartz (Qtz), BLF-11b, BSE

(0.40% $V_2O_3$) but not in titanium. In contrast, late hematite in the breccia cement (Fig. 7b) contains 6 mol% ilmenite in solid solution (ESM App. 6).

## Oroya Stage 1 sulfides and tellurides

The breccia ore of the Flat Lode (Stage 1 + 2?) contains about 5 vol% disseminated pyrite, many grains zoned (Fig. 7a) to poikilitic arsenical rims (≤ 1.97 wt% As; ESM App. 7). Chalcopyrite is accessory. Grains of native gold (< 1 to 15 μm) are attached to pyrite surfaces and enclosed in pyrite, commonly along growth zones lined with hematite (Fig. 7c). Some inclusions may be unidentified telluride. The gold is pure Au–Ag alloy and has a fineness of 909 (ESM Table 2). The Stage 1 gold in the Blatchford and OHW lodes has an average fineness of 895 but is alloyed with mercury (ESM Table 2). The silver (10.16–20.31 at%) and mercury contents (0.10–0.80 at%) vary from grain to grain.

**OHW Lode** The mylonite and breccia ore contains pyrite (10–15 vol%) less than 5 μm to 3 mm in size. In chert-like quartz, subhedral grains and dendritic pyrite aggregates are associated and in contact with arsenopyrite and sphalerite (1 vol% each), lesser chalcopyrite and rare gersdorffite (Fig. 7d, e). Locally, euhedral arsenopyrite is enclosed in pyrite together with anhedral pyrrhotite (Fig. 7f). Native gold (< 1 to 32 μm) forms inclusions in pyrite and arsenopyrite (Fig. 7g), fills fractures in both together with melonite (Fig. 7h) and occurs attached to the surfaces of all sulfides.

The average pyrite is low in As, Ni and Co (< 0.12 wt%). A few grains have cores enriched in Ni (≤ 1.54%) and Co (≤ 0.42%), whereas others contain arsenical zones (≤ 0.83% As) in either core or rim (ESM App. 7). The sphalerite (average 1.88 at% Fe) encloses blebs of chalcopyrite. The chalcopyrite contains trace Co in solid solution and, locally, sphalerite and telluride inclusions (ESM App. 9). In arsenopyrite, Co and Ni are low (< 1 wt% combined) and Sb is below detection (ESM App. 10).

**Blatchford Lode** The chert-like quartz in the Blatchford shear zone and the chalcedony margin of the extension vein contain pyrite (7–15 vol%) in contact with pyrrhotite (0.5–3%) and arsenopyrite (0.5%). The three phases form equilibrium assemblages (Fig. 8a) associated with native gold and melonite (Fig. 8b). Pyrrhotite has low average Co and Ni contents (0.06–0.12 wt%). Arsenopyrite is consistently enriched in Co (up to 4.02%), the cobalt content decreasing from core to rim in the shear zone but not in the vein. Micron-sized inclusions of gold and telluride were detected in both sulfides (ESM App. 10).

Pyrite–pyrrhotite contacts vary from mutual (in equilibrium) to embayed where pyrrhotite is replaced by finely granular pyrite (Fig. 8c, d) or by rare marcasite (Fig. 8e). Some aggregates are zoned from solid rims to granular cores (Fig. 8f) indicating the total replacement of early pyrrhotite. Pyrite also forms complex aggregates in chalcedony zoned from crystal cores to dendritic rims (Fig. 8g). On average, As, Ni and Co are low (< 0.3 wt%). Nickel is locally enriched (up to 1.69%; ESM App. 7).

Chalcopyrite and sphalerite (0.5 vol% each) are in contact with the iron sulfides (Fig. 8c). Rare ullmannite (Fig. 8h; ESM Table 1) occurs in veinlets adjacent to the main shear zone. Chalcopyrite contains Co in solid solution (< 0.08 wt%) and rare inclusions of sphalerite and native gold. Sphalerite in contact with pyrite or pyrite + pyrrhotite is rich in iron (5.21–5.73 at%) and encloses chalcopyrite blebs and micron-sized grains of gold telluride and bismuth sulfide (ESM App. 9).

**Fig. 7** Oxides, sulfides, tellurides and gold in Oroya Stage 1 ore from the Flat Lode (**a**–**c**; part Stage 2?) in propylitic Golden Mile Dolerite, North Kalgurli shaft 13 level, and from the OHW Lode (**d**–**h**) in sericite–ankerite-altered Paringa Basalt, Paringa South shaft 7 level, photomicrographs in plane polarised light reflected in air (PPL) and backscattered electron (BSE) images. **a** Magnetite (Mag) in contact with pyrite (Py), which is zoned to As-rich poikilitic rims, sample FLO-2, PPL. **b** Fractured pyrite (Py) rimmed and cemented by hematite (Hem) containing 6 mol% ilmenite (ESM App. 6), FLO-2, PPL. **c** Pyrite (Py) growth zones (rim = Stage 2?) separated by carbonate (black) and hematite (Hem), 20 grains (white, < 1 to 10 μm) of native gold (Au) and telluride (?) are enclosed in pyrite, FLO-2, BSE. **d** Fractured arsenopyrite (Asp) associated with euhedral and dendritic pyrite (Py), sphalerite (Sp) and chalcopyrite (Ccp), OHW-8b, PPL. **e** Gersdorffite (Gsd; ESM Table 1) in contact with chalcopyrite (Ccp), OHW-6, PPL. **f** Thermometry assemblage: pyrite (Py) containing inclusions of pyrrhotite (Po) and arsenopyrite (Asp). The BSE image (**g**) is outlined in red, OHW-22a, PPL. **g** Close-up view of **f**: arsenopyrite (Asp), pyrrhotite (Po), melonite (Mln; EDS 29 at% Ni, 59% Te) and native gold (Au; EDS 75 at% Au, 12% Ag, 11% Hg, 2% Bi) enclosed in pyrite (Py), OHW-22a, BSE. **h** Native gold (Au) and melonite (Mln; EDS 28 at% Ni, 58% Te) line a fracture in pyrite (Py), OHW-22a, PPL

## Oroya Stage 2 sulfides and tellurides

On the Paringa South shaft 4 to 11 levels, Stage 2 sulfide–telluride ore (Au/Ag = 3.8–6.9) occurs in crosscutting breccia and vein networks in the OHW Lode and Oroya Shoot and in the Blatchford extension vein (Mueller 2018; Mueller and Muhling 2019). The OHW and Blatchford ore bodies contain subhedral pyrite (3–5 vol%), sphalerite, chalcopyrite and arsenopyrite (0.5% each). The sulfides are in contact with free gold and a Pb–Sb-rich suite of tellurides including montbrayite, calaverite, altaite, tellurantimony, coloradoite and minor petzite and melonite (ESM Table 2; App. 11). The pyrite contains inclusions of native gold and telluride, and adjacent free tellurides are in equilibrium contact with each other and with gold (Fig. 9a–e; ESM App. 12). Replacement textures are absent.

Stage 2 pyrite contains As (< 0.9 wt%) and Co (< 0.5%) in solid solution (ESM App. 7). Sphalerite associated with pyrrhotite in the Blatchford vein is more iron-rich (average 3.55 at% Fe) than Stage 2 sphalerite in the Oroya Shoot on the Paringa South shaft 4 level (1.92 at%), which is similar in composition to Stage 1 sphalerite in the OHW Lode on 7 level (1.88 at%; ESM App. 9). Chalcopyrite blebs and trace mercury are common in Stage 2 sphalerite, whereas most chalcopyrite is inclusion-free.

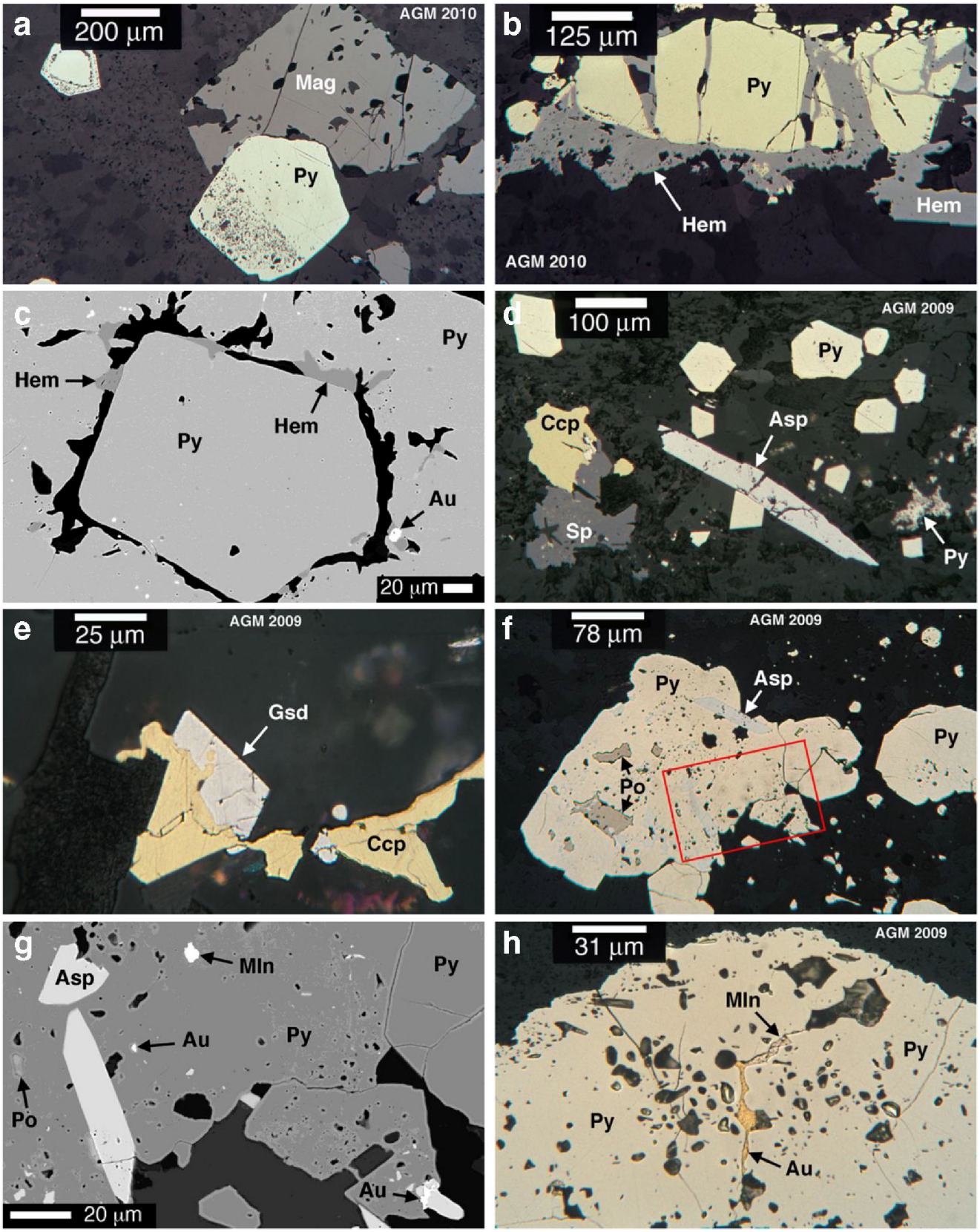
a
200 μm
AGM 2010
Mag
Py
b
125 μm
Py
Hem
Hem
AGM 2010
c
Py
Hem
Hem
Py
Au
20 μm
d
100 μm
AGM 2009
Py
Ccp
Asp
Sp
Py
e
25 μm
AGM 2009
Gsd
Ccp
f
78 μm
AGM 2009
Py
Asp
Py
Po
g
Asp
Mln
Py
Au
Py
Po
Au
20 μm
h
31 μm
AGM 2009
Mln
Py
Py
Au

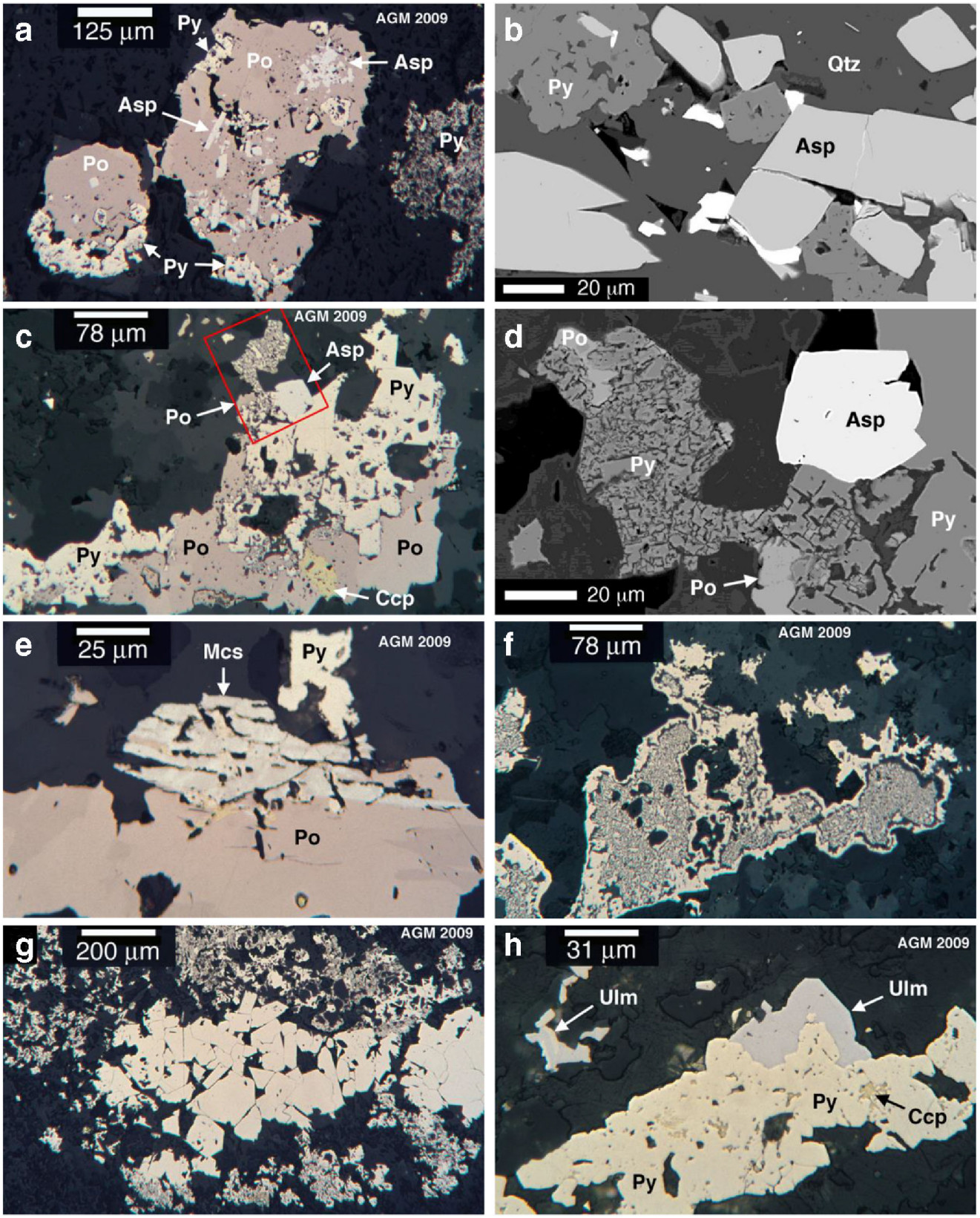
a
125 μm
Py
Po
Asp
Asp
Py
Po
Py
AGM 2009
b
Qtz
Py
Asp
20 μm
c
78 μm
AGM 2009
Asp
Py
Po
Py
Po
Po
Ccp
d
Po
Asp
Py
Py
20 μm
Po
e
25 μm
Mcs
Py
AGM 2009
Po
f
78 μm
AGM 2009
g
200 μm
AGM 2009
h
31 μm
AGM 2009
Ulm
Ulm
Py
Ccp
Py

◀ **Fig. 8** Sulfides, tellurides and gold in Oroya Stage 1 ore from the Blatchford shear zone and extension vein in sericite–ankerite-altered Paringa Basalt, Paringa South shaft 11 level, photomicrographs in plane polarised light reflected in air (PPL) and backscattered electron (BSE) images. **a** Thermometry assemblage in vein: pyrrhotite (Po) in contact with subhedral pyrite (Py) and arsenopyrite (Asp) adjacent to dendritic pyrite in chalcedony, sample BLF-11c, PPL. **b** Vein: melonite (EDS 31.8 at% Ni, 65.1% Te) and native gold (both white) in contact with arsenopyrite (Asp) and pyrite (Py) in chalcedony (Qtz), BLF-11c, BSE. **c** Thermometry assemblage in shear zone: pyrite (Py) in contact with arsenopyrite (Asp), pyrrhotite (Po) and chalcopyrite (Ccp). The BSE image (**d**) is outlined in red, BLF-7a, PPL. **d** Close-up view of **c**: replacement of pyrrhotite (Po) by granular pyrite (Py), the arsenopyrite (Asp) was in contact with pyrite + pyrrhotite, BLF-7a, BSE. **e** Vein: marcasite (Mcs) replacement in pyrrhotite (Po), adjacent pyrite (Py), BLF-2c, PPL. **f** Shear zone: pyrite aggregates zoned from solid rims to granular cores, the granular texture indicates replacement of pyrrhotite, BLF-7b, PPL. **g** Vein: pyrite aggregate zoned from subhedral crystals to an outer dendritic margin in chalcedony, BLF-2c, PPL. **h** Shear zone: ullmannite (Ulm; ESM Table 1) in contact with pyrite (Py) enclosing chalcopyrite (Ccp), BLF-8, PPL

Tetrahedrite and digenite–covellite–bornite aggregates (0.1–0.2 vol%) are part of the assemblage in the Blatchford vein (Fig. 9f, g). Covellite and digenite also rim Stage 1 chalcopyrite in the OHW Lode adjacent to Stage 2 veins (Fig. 9h). The tetrahedrite has a low tennantite component (atomic ratio Sb/As = 43) and contains Fe, Zn and Ag in solid solution. Bi, Hg and Se were detected locally (ESM Table 1). Covellite and digenite both contain iron (0.76–3.90 wt%) substituting for copper, and covellite in the Blatchford vein contains minor silver (ESM Table 1).

Stage 2 native gold has an average fineness of 931 (11.9 at% Ag), but silver varies from grain to grain (6.5–18.3 at%). Other alloyed metals (Hg, Bi) and pyrite and telluride inclusions were detected locally (ESM Table 2). The principal gold telluride is montbrayite [mean: $(Au_{21.81}Sb_{1.19})(Te_{34.32}Sb_{3.68})$; formula after Bindi et al. 2018] in contact with calaverite $[(Au_{0.88}Ag_{0.05}Sb_{0.07})(Te_{1.88}Sb_{0.12})]$ distinguished by its silver content (ESM Table 2; Fig. 9c–e). Petzite partly decomposed under the 20-nA electron beam of the microprobe resulting in non-stoichiometric WDS analyses (ESM Table 2). Under the low-energy beam used during EDS analysis, its composition was close to ideal ($Ag_3AuTe_2$; ESM App. 8). Tellurantimony ($Sb_2S_3$) always contains small amounts of lead in solid solution, and altaite (PbTe) and coloradoite (HgTe) incorporate minor antimony. Silver is locally present in all three (< 0.4 wt%; ESM App. 11). In melonite ($NiTe_2$), minor Co and lesser Fe and Sb substitute for nickel (ESM Table 2).

## Temperature–pressure estimates

Oroya Stage 1 arsenopyrite was analysed in two samples from the OHW Lode containing pyrite–arsenopyrite and pyrite–pyrrhotite–arsenopyrite assemblages. The average temperature calculated from 6 to 10 analyses (< 1 wt% Co + Ni + Sb) is remarkably consistent: 398 °C (2-phase), 392 °C (2-phase cores), 403 °C (2-phase rims), 408 °C (3-phase) and 410 °C (3-phase). The same consistency is evident in a sample from the Blatchford vein: 429 °C (2-phase), 432 °C (3-phase), 436 °C (3-phase cores) and 434 °C (3-phase rims). High-Co arsenopyrites (> 1 wt% Co ± Ni) give higher temperatures: OHW Lode 439 °C (2-phase), Blatchford Lode 448 °C (3-phase) and 455 °C (3-phase). In summary, the median temperature of 420 ± 30 °C is considered the most reliable estimate for Oroya Stage 1 ore (ESM Table 3).

### Chlorite thermometry

Temperatures calculated according to Cathelineau (1988) for 8 to 20 chlorite grains per sample varied ± 12 to ± 32 °C ($2\sigma$) about the average. The wider spread of the Kelly Lode sample (± 48 °C), still within the error of calibration (± 50 °C; Lanari et al. 2014), is attributed to a mixture of remnant propylitic (340 °C) and ore-related chlorite in contact with pyrite (400 °C; ESM Table 3). Four samples taken across the OHW Lode allowed checks on consistency. Oroya Stage 1 chlorite (Mg number = 0.26–0.49) gave tightly grouped temperatures ranging from 409 ± 18 to 423 ± 20 °C ($2\sigma$ precision). The temperature estimates based on Lanari et al. (2014) are outside the calibration range (> 500 °C) in two cases (ESM Table 3). In the OHW Lode, they are at odds with arsenopyrite thermometry. In the Flat Lode, they are too high to account for the low amount of ilmenite (6 mol%) in Ti-hematite (Braun and Raith 1985). Thus, the calibration of Cathelineau (1988) is preferred as it provides consistent estimates in agreement with arsenopyrite thermometry (ESM Table 3): 340 °C for propylitic alteration below the Kelly Lode, 370–400 °C for Fimiston ore in the Kelly and B-Lode, 385 ± 50 °C for late-stage Oroya ore in the Flat Lode, 400–420 °C for Oroya Stage 1 and 380–400 °C for Stage 2 ore in the OHW and Blatchford lodes.

### Sulfide–telluride thermometry

Rare marcasite replacing pyrrhotite in Oroya Stage 1 ore of the Blatchford vein suggests temperatures < 425 °C (Qian et al. 2011). Stage 2 altaite–tellurium myrmekite in the Oroya Shoot on 4 level (Mueller and Muhling 2019) and in the Blatchford Lode on 10 level (Scantlebury 1983), interpreted to represent the solid-state exsolution of trapped melt, indicates deposition above the eutectic at 411 °C (Lin et al. 1989).

In the No. 4 and Phantom lodes (see ESM Fig. 1), the occurrence of krennerite suggests that many tellurides

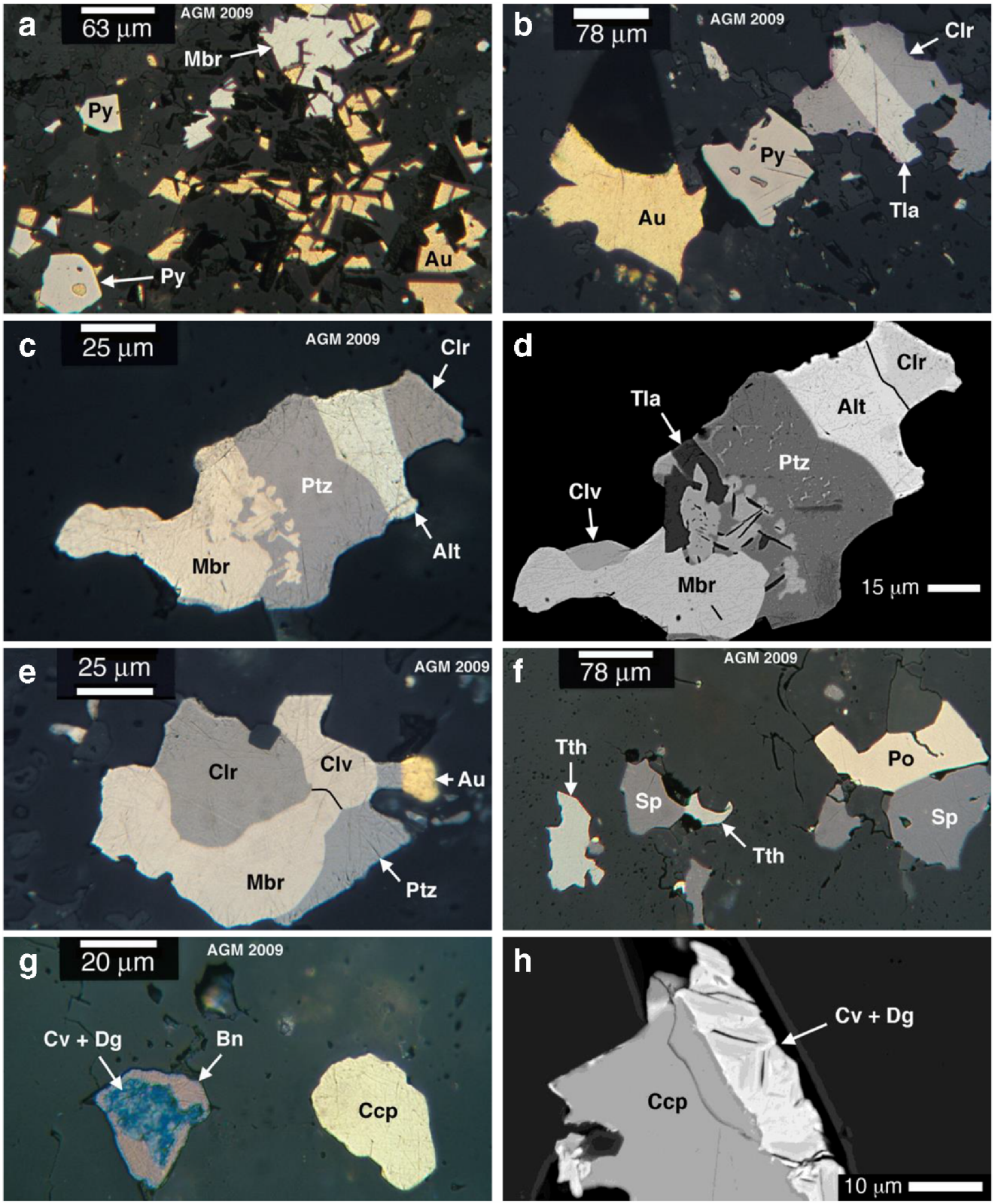


crystallised below 380 °C. The silver content of krennerite in the No. 4 Lode (3.1–6.2 wt%) agrees well with experimental values (3.3–6.2 ± 0.2%) at 380–350 °C (Cabri 1965). Sylvanite surrounding krennerite (Baker 1958) indicates

◀ **Fig. 9** Sulfides, tellurides and gold in Oroya Stage 2 ore from the OHW Lode (**a**, **h**) and Blatchford extension vein (**b**–**g**) in sericite–ankerite-altered Paringa Basalt, Paringa South shaft 7 and 11 levels, photomicrographs in plane polarised light reflected in air (PPL) and backscattered electron (BSE) images. **a** Native gold (Au) interstitial to muscovite + quartz in contact with montbrayite (Mbr) and pyrite (Py), sample OHW-22b, PPL. **b** Native gold (Au), pyrite (Py; coloradoite inclusions), tellurantimony (Tla) and coloradoite (Clr), BLF-2c, PPL. **c** Equilibrium assemblage (ESM App. 12) of montbrayite (Mbr), petzite (Ptz), altaite (Alt) and coloradoite (Clr). Calaverite, tellurantimony and montbrayite are close in colour and reflectance, BLF-11b, PPL. **d** Assemblage as in **c**: Montbrayite (Mbr) in contact with calaverite (Clv), tellurantinomy (Tla) and petzite (Ptz), which is in contact with altaite (Alt), outer coloradoite (Clr). The petzite encloses blebs of calaverite and plates of muscovite (black), BLF-11b, BSE. **e** Equilibrium assemblage (ESM App. 12) of montbrayite (Mbr), calaverite (Clv), coloradoite (Clr), petzite (Ptz) and native gold (Au), BLF-2c, PPL. **f** Pyrrhotite (Po) in contact with sphalerite (Sp), and sphalerite with tetrahedrite (Tth), BLF-11a, PPL. **g** Aggregate zoned from a covellite–digenite core (Cv + Dg; ESM Table 1) to a bornite rim (Bn) adjacent to chalcopyrite (Ccp), BLF-11b, PPL. **h** Covellite (Cv) + digenite (Dg; ESM Table 1) replacement rim on Stage 1 chalcopyrite (Ccp), OHW-11a, BSE

cooling to below 350 °C (Cabri 1965). The presence of realgar crystals in the upper No. 4 Lode (< 760 m depth) and of Ag-rich covellite ($Cu_{1.01–1.23}Ag_{0.15–0.31}S$; Golding 1978) 1200 m below the surface suggest fluid cooling to < 310 °C. Realgar melts at 307 ± 5 °C, and covellite + argentite$_{s.s.}$ melt incongruently at 325 ± 25 °C (Barton and Skinner 1979). The melting temperatures quoted, determined at 1 bar and dry conditions, increase with pressure by about 14 °C/kbar (Sharp et al. 1985), whereas aqueous fluid diffusing into immiscible melt will lower the solidus (Cabri 1965).

### Pressure estimates

Barometry based on mineral assemblages in the Hannan South Cu–Au skarn 12 km southeast of Kalgoorlie provides an estimate of 440 ± 120 MPa (1$\sigma$) for replacement in D3 reverse faults (Mueller et al. 2012), a structural setting time equivalent to that of the Oroya ore bodies. Fluid inclusion data constrain the median and maximum isochore pressures to 280 and 400 MPa in D2a Fimiston Lodes and to 180 and 280 MPa in D3a Oroya Lodes (Ho et al. 1990). Fluid inclusions in Oroya-style hematite–pyrite ore from the North Kalgurli Flat Lode homogenised at maximum temperatures of 235–240 °C (Ho et al. 1990), 150 °C lower than estimated from chlorite thermometry (ESM Table 3). If this fluid was trapped as a single phase, the pressure calculated for the system $H_2O$–$CO_2$–NaCl would be 300 MPa at 350 °C and 380 MPa at 400 °C (ESM App. 13). The results suggest a pressure of at least 200 MPa, most probably 300 MPa for ore formation in the Golden Mile, corresponding to a depth of 7–11 km below the surface at lithostatic load (3.6 km per 100 MPa; Bucher and Frey 2002).

## Discussion

The mineralogical and thermometric data presented above for representative ore bodies in the Golden Mile are summarised in Fig. 10. The pressure–temperature estimates are discussed first in comparison to those from other gold deposits, as they provide constraints on fluid composition (pH, oxygen, sulfur and tellurium fugacity) and fluid evolution during ore deposition. These constraints are integrated with those imposed by potential fluid sources, in particular the monzodiorite-suite plutons represented by porphyry dykes at Kalgoorlie (Mueller 2017; this issue). Key features of the Miocene Porgera gold deposit in Papua New Guinea are reviewed, as many are shared with the Golden Mile.

### *P–T* regime of ore formation

The Golden Mile has been interpreted as an epithermal deposit (250–170 °C, 10–50 MPa; Clout 1989), especially with regard to the Oroya-style telluride ore (300–170 °C; Shackleton et al. 2003). Gauthier et al. (2007) also infer a "high crustal level (< 7 km and likely much shallower)" based on the occurrence of chalcedony and cockade breccia. In contrast, the results presented above indicate two superimposed hydrothermal systems (Fig. 10), peak fluid temperatures of 420 ± 30 °C, main-stage ore deposition from supercritical fluids at 400–350 °C, minor deposition during cooling to 300 °C and a mid-crustal level of mineralisation (7–11 km depth). Temperature estimates for other mesothermal gold deposits in the wider Kalgoorlie area are 420–250 °C (Mikucki and Ridley 1993), and 480 ± 60 °C for biotite–pyrite–anhydrite alteration at porphyry dykes below the East Repulse gold deposit (Bath et al. 2013). The presence of kyanite in some gold-related alteration zones indicates 250–400 MPa pressure and deep erosion since ore formation in the Eastern Goldfields fold belt (Mueller 2018).

### Fluid composition and pH

The Fimiston and Oroya hydrothermal fluids were both of low to moderate salinity (1.0–5.5 wt% $NaCl_{eq}$), high density (0.75–0.95 g/cm$^3$) and varied in mole fraction $CO_2$ from 0.05 to 0.25 (median = 0.15). Methane ($X_{CH4}$ = 0.02–0.06) was detected in veins where the D3a Oroya shear zones intersect altered carbonaceous greywacke (Ho et al. 1990). At 200–300 MPa pressure, ore deposition took place at supercritical conditions from fluids not separated into liquid and vapour (Fig. 11a).

The Fimiston Lodes are composed of Fe–dolomite–albite vein selvages, which grade into ankerite–phengite–quartz zones replacing propylitic Golden Mile Dolerite.

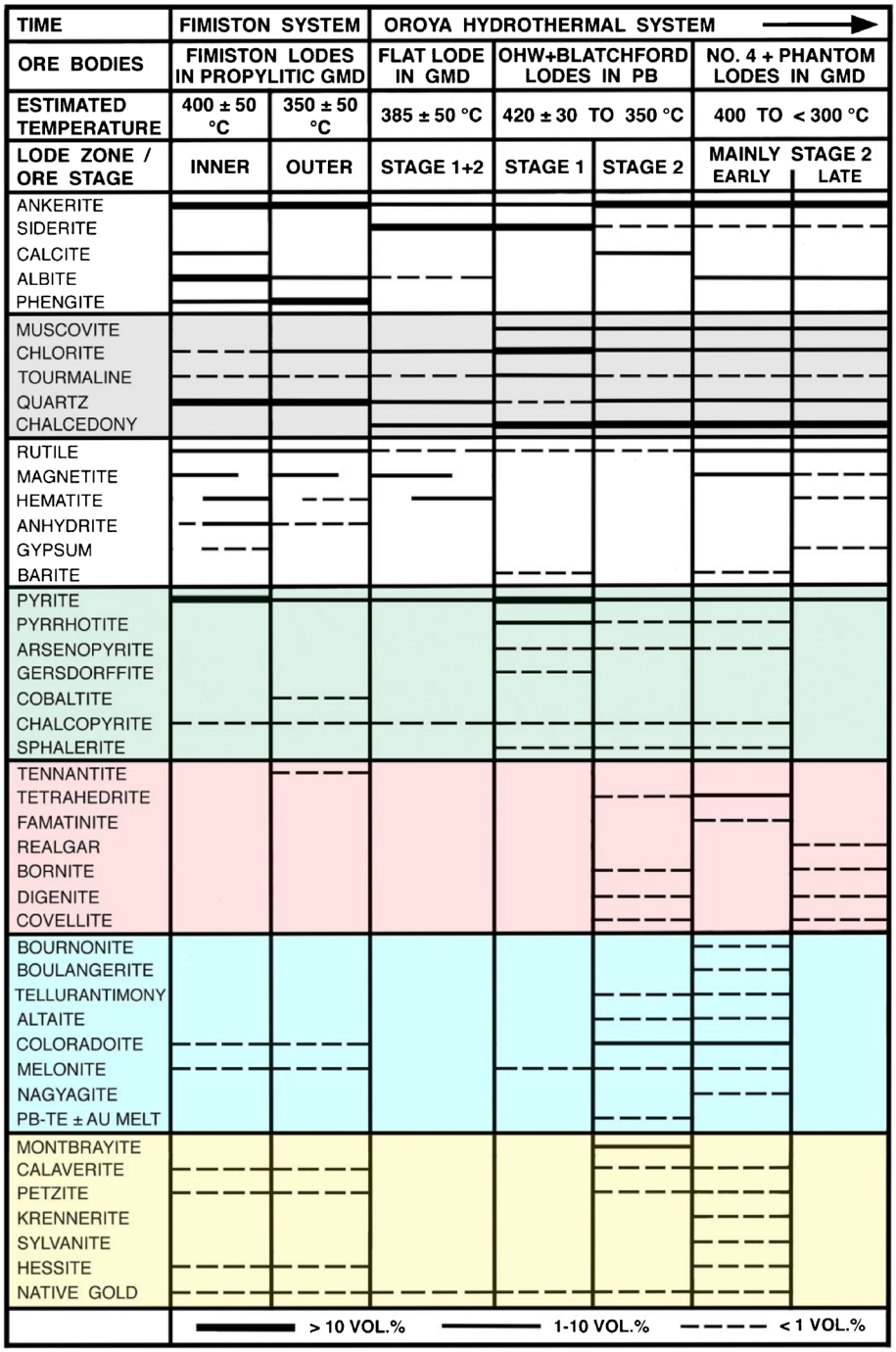


**Fig. 10** Paragenetic diagram summarising the mineralogy of Fimiston- and Oroya-style gold ore in the Golden Mile deposit, Kalgoorlie. Oroya-style mineralisation overprints Fimiston ore in many D2a and some D2b faults and is the only ore type in D3a reverse faults (Mueller 2017, 2018). The correlation of late pyrite + hematite + gold in the D3a Flat Lode with Oroya Stage 2 telluride ore is preliminary. Mineral data from the D2a Horseshoe No. 4 and Phantom lodes are reviewed in ESM Fig. 1. The term "quartz" denotes granular, columnar and comb-textured crystals, and "chalcedony" includes recrystallised chert-like silica. The ore minerals are grouped into: (1) sulfides and sulfarsenides (green); (2) Cu–As–Sb sulfosalts, realgar and Cu-sulfides (red); (3) Pb–Sb sulfosalts, Pb–Sb tellurides, coloradoite and melonite (blue); and (4) Au–Ag tellurides and native gold (yellow). Gold ore replacing propylitic Golden Mile Dolerite (GMD) is refractory (Fimiston Lodes; Oroya-style Flat Lode), because gold and tellurides form micron-sized inclusions in pyrite. Oroya-style ore replacing ankerite-rich rock in the Paringa Basalt (PB) contact zone and in reactivated Fimiston Lodes is mostly free milling

Albite in the veins and selvages buffered the fluid pH to neutral values of 5 to 5.5, whereas the assemblage mica + quartz in the outer zone suggests more acidic pH values of 4–5 assuming 1–5 wt% NaCl in the fluid (Fig. 11b, c). In the outer zone, the hydrogen ions required to alter propylitic albite were released during the selective replacement of propylitic chlorite [Fe/(Fe + Mg) = 0.5] by ankerite [Fe/(Fe + Mg) = 0.3–0.4] and pyrite:

$$(MgO, FeO)_{chlorite} + Ca^{2+} + 2\,H_2CO_3{}^0 + 2\,H_2S_{aq} = Ca\,(Mg_{0.65}, Fe_{0.35})\,(CO_3)_2 + FeS_2 + 4\,H^+ + 2\,H_2O \quad (1)$$

The Fe/(Mg + Fe) ratios of chlorite and ankerite, written in this simplified carbonation–sulfidation reaction for average

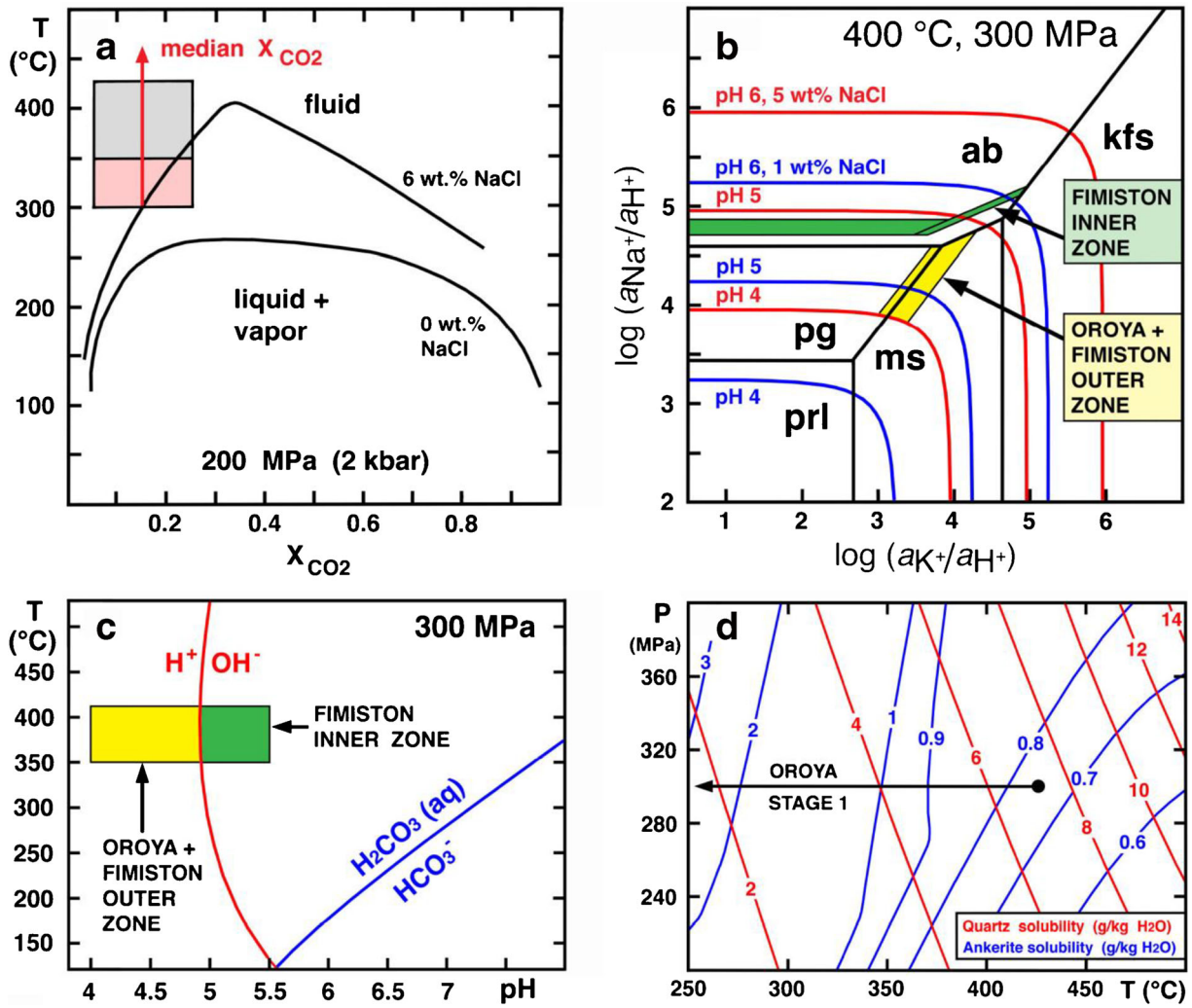


**Fig. 11** PTX diagrams illustrating hydrothermal conditions during the formation of Fimiston- and Oroya-style gold ore, Golden Mile, Kalgoorlie. **a** *T*–$X_{CO2}$ phase diagram at the minimum estimated pressure of 200 MPa for $H_2O$–$CO_2$ fluids of 6 wt% NaCl and 0 wt% NaCl salinity (modified from Robert and Kelly 1987). The *T*–$X_{CO2}$ range is from Ho et al. (1990) and data in ESM Table 3. Fluids were supercritical (grey field), and phase separation was restricted to local extensional structures (red field). **b** Stability relationships at unit activity (black lines) of albite (ab), paragonite (pg), K-feldspar (kfs), muscovite (ms) and pyrophyllite (prl) as a function of fluid composition ($X_{CO2}$ = 0.15) in the presence of quartz. The $pH_T$ contours (at pH = 4, 5, 6) are for salt activities ($Na^+ + K^+$) of 0.173 and 0.90 corresponding to 1 wt% (blue lines) and 5 wt% NaCl (red lines) in solution. The activities of muscovite and paragonite (ESM App. 4) in the Fimiston Kelly Lode and B-Lode (green field) and the Oroya OHW and Blatchford lodes (yellow field) constrain the fluid pH during albite-stable and hydrolitic alteration, respectively. **c** *T*–pH diagram showing the estimated pH range of the fluids depositing Golden Mile ore, the predominance boundary $H^+$ versus $OH^-$ (neutral pH), and the dissociation equilibrium $H_2CO_3(aq) = HCO_3^- + H^+$ at 300 MPa pressure. **d** *P*–*T* diagram showing the solubilities of quartz and ankerite in a supercritical $H_2O$–$CO_2$ fluid ($X_{CO2}$ = 0.15) of moderate salinity (5 wt% $NaCl_{eq}$), and the cooling path during the replacement of early ankerite by Oroya Stage 1 chalcedonic silica. The diagram was calculated for fluid in contact with quartz + ankerite [$Ca(Mg_{0.5}Fe_{0.5})(CO_3)_2$] using HCh and the Unitherm database (Shvarov 2008), and treating ankerite as an ideal solid solution between $CaMg(CO_3)_2$ and $CaFe(CO_3)_2$ using properties listed in Zimmer et al. (2016)

Kelly and B-Lode compositions, vary with MgO and FeO in Units 1 to 10 of the GMD sill.

In the Oroya-style OHW and Blatchford Lodes, hosted by sericite–ankerite-altered Paringa Basalt, albite is rare or absent. The assemblage K-Na muscovite + quartz indicates a moderately acidic pH of about 4 for the input fluid (Fig. 11b, c). Minor late-stage albite in the Flat Lode and No. 4 Lode suggests an evolution to a near-neutral pH with time. The dissociation of $H_2CO_3$ (aqueous) had no effect (Fig. 11c).

## Replacement silica

Chalcedony veins and replacement silica are common in epithermal Au–Ag deposits. The precipitation of

chalcedony requires rapid cooling and super-saturation of silica in the fluid, conditions associated with boiling (Fournier 1985). Replacement silica–pyrite "jasperoid" is also widespread in Carlin-type gold deposits and is present in sericite alteration zones associated with intrusion-related Cu–Mo–Au deposits (Barton et al. 1997). In the Carlin-type deposits, jasperoid formed at 180–240 °C by carbonate dissolution and silica precipitation in sedimentary host rocks during the interaction with acidic, low-salinity (≤ 6 wt% $NaCl_{eq}$) $H_2O$–$CO_2$ fluids showing no evidence of boiling (Muntean 2018).

Chert-like quartz or chalcedony, dark grey due to enclosed pyrite, distinguishes Oroya- from Fimiston-style ore. In many Fimiston Lodes, chalcedonic quartz formed replacement zones (3.4–5.2 g/t Au) brecciated and cemented by light grey quartz + carbonate containing native gold and tellurides (Tomich 1952). These relationships are observed in the Paringa South mine and termed Oroya Stage 1 and Stage 2 (Fig. 10). Older hydrothermal ankerite in the Paringa Basalt contact zone and in Fimiston Lodes was replaced by chalcedonic quartz, a process promoted by an acidic pH and by the retrograde solubility of ankerite as the fluid infiltrated the wall rock and cooled (Fig. 11d). A slight super-saturation of silica and iron in the fluid is indicated by the presence of dendritic pyrite in chalcedony (Fig. 8a, g). Rapid cooling of the Stage 1 input fluid (420 ± 30 °C) was possible due to the low ambient temperature of the wall rocks, estimated at 250 °C at 10 km depth given a geothermal gradient of 25 °C/km in the greenstone belt (Mueller et al. 2016; this issue).

## Fluid evolution from the source

The oxide–sulfide assemblages in Golden Mile ore (Fig. 10) have been interpreted to reflect the infiltration of a reduced metamorphic fluid (Goldfarb et al. 2005) oxidised by reaction with Ti-magnetite in the Golden Mile Dolerite sill (Evans et al. 2006). The destruction of the magnetite component during greenschist-facies metamorphism and propylitic alteration prior to ore deposition and the low amount of remnant Ti-magnetite (< 1 vol%) relative to ferrous chlorite (40–50 vol%) available to buffer the fluid are inconsistent with this interpretation. Alternatively, the oxidised fluids were sourced from I-type plutons in the composite batholiths emplaced into the Kalgoorlie Terrane. In the Archean Wyoming Province, USA, calc-alkaline intrusions in the Louis Lake batholith released low-salinity $H_2O$–$CO_2$ and high-salinity aqueous fluids at crystallisation pressures > 300 MPa, which formed lode gold deposits and copper-rich veins in the adjacent greenstone belt (Vaughn and Ridley 2014).

As argued in other contributions to this issue, mass-balance calculations, strontium isotope and stable isotope data implicate the parent plutons of the monzodiorite-suite stocks and dykes emplaced along the Boulder Lefroy–Golden Mile fault system as the source of the auriferous fluids. Hornblende compositions indicate that the I-type calc-alkaline melts had high water contents (3–6 wt% $H_2O$) and oxidation states (log $f_{O2} = -11.3$ to $-12.8$ at 750–850 °C). In log $f_{O2}$–$T$ space, these constraints place the intrusions on the isomolar $SO_2$–$H_2S$ buffer curve (Fig. 12a), consistent with the sulfate in apatite (0.14–0.37 wt% $SO_3$), which suggests trace igneous anhydrite (Mueller et al. 2016). Fluid exsolved from such melts may have positive bulk $\delta^{34}S$ values of up to 5‰ (Manalo et al. 2018) and evolve along the $SO_2$–$H_2S$ buffer to sulfur contents of 0.1 to 0.01 wt% at 500–400 °C (1 to 0.1 mol ΣS; Ohmoto 1986).

The Hannan South Cu–Au endoskarn southeast of Kalgoorlie formed from such a magmatic fluid, which became reduced by interaction with the porphyry wall rocks as it cooled and moved away from its source (Fig. 12a). In the Golden Mile, the late hematite–pyrite ore in the Fimiston-style B-Lode and in the Oroya-style Flat Lode may record the oxidation state of the input fluids, because this ore was deposited after most interaction with chlorite in the GMD host rock had ceased. Organic methane released from carbonaceous greywacke and interflow shales (Simpson 1912) and trapped in fault zones (Blatchford, OHW, No. 4 lodes) caused a sharp reduction of the Oroya Stage 1 $H_2O$–$CO_2$ fluid stabilising pyrrhotite at oxygen fugacities trending towards the $CO_2$–$CH_4$ buffer (Fig. 12a). Again, this effect waned with time and the Oroya Stage 2 fluid was mainly buffered by pyrite + magnetite, the oxidation state increasing in the No. 4 Lode during the deposition of late hematite (Fig. 12a).

## Fluid oxidation–sulfidation state during mineralisation

The oxidation–sulfidation state of the aqueous–carbonic fluids during mineralisation is constrained by the iron sulfide–iron oxide assemblages observed and by the ferrous iron in dolomite–ankerite and siderite, the most abundant gangue minerals. Thermodynamic calculations indicate that the ferroan dolomite–calcite assemblage, present in fault-fill veins of the Kelly Lode (Fimiston), Blatchford shear zone (Oroya Stage 1) and Blatchford vein (Oroya Stage 2), is stable at 420 °C (Fig. 12b). The stability of iron-rich carbonates increases sharply at lower temperature (Fig. 12c). Consequently, siderite and ankerite predominate in the chalcedony "chill" zone of the Blatchford vein and in the carbonate–chlorite cement of silica breccia in the OHW Lode (both Oroya Stage 1). The common zonation of carbonates to iron-rich rims is probably also due to the decline of temperature with time. However, the reverse zonation to

Mg-rich rims coincident with hematite + pyrite in the Fimiston-style B-Lode and the Oroya-style Flat Lode suggests a competing effect related to the increased oxidation state of the fluid.

In Fimiston-style ore, ankerite is much more abundant than siderite because the Fimiston fluid introduced calcium but not iron (Mueller 2018). During wall-rock infiltration, ankerite compositions were controlled by the Fe/(Mg + Fe) ratio of the propylitic chlorite replaced, by the co-precipitation of pyrite ± magnetite and finally by declining temperature. The phase relations indicate that calcite + Fe-dolomite remained stable relative to anhydrite during high-$T$ pyrite–magnetite mineralisation and that ankerite + anhydrite were stable during lower-$T$ pyrite + hematite, when chlorite replacement ceased and the oxidation state was buffered by $H_2S$–$HSO_4^-$ in the input fluid (Fig. 12b, c).

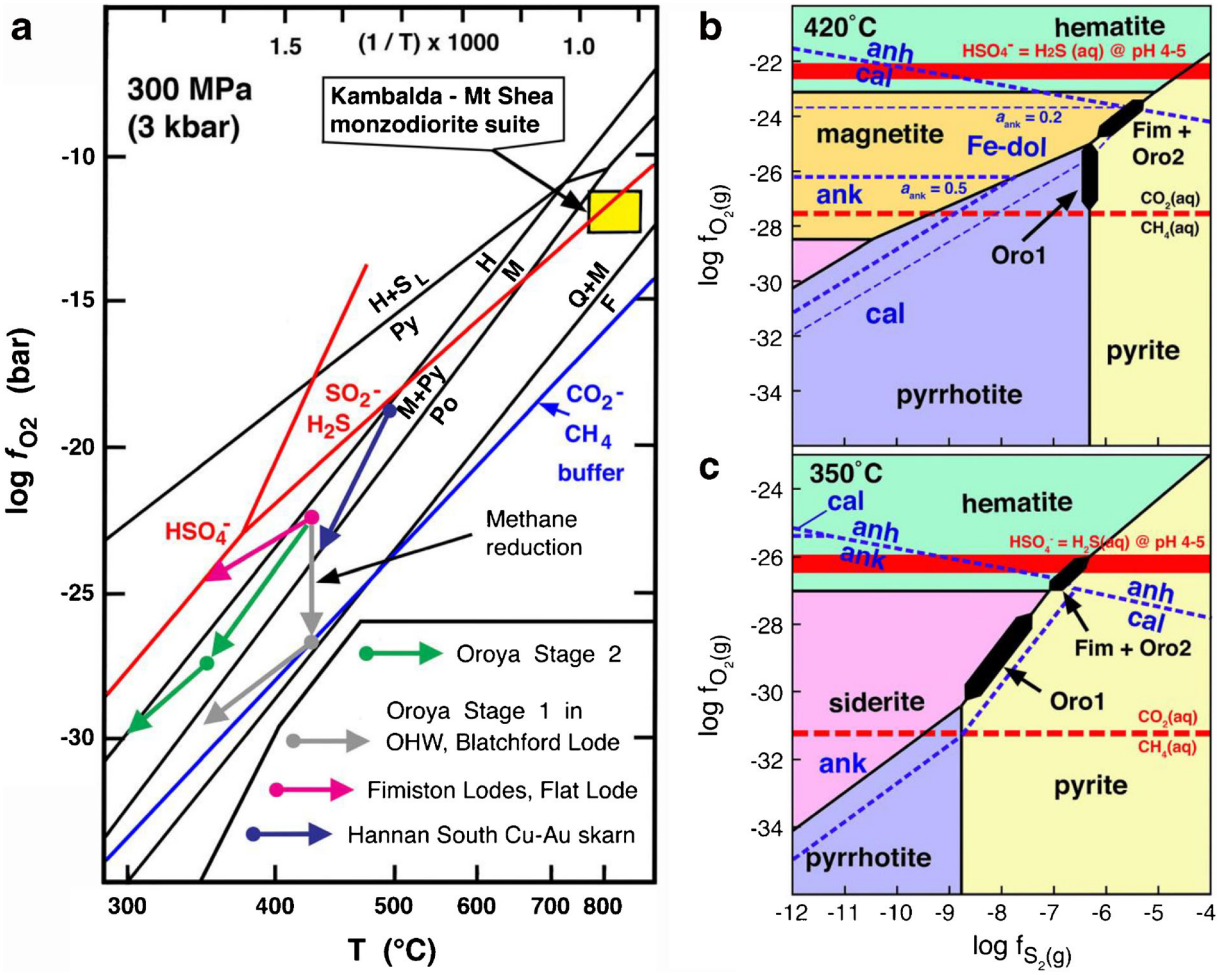


**Fig. 12** Diagrams at 300 MPa pressure constraining the oxidation/sulfidation state and evolution of hydrothermal fluids during mineral deposition in Fimiston- and Oroya-style ore, Golden Mile, Kalgoorlie. **a** Log $f_{O2}$–$T$ diagram (modified from Ohmoto 1986) showing the calculated magmatic fluid (Mueller et al. 2016) of local I-type monzodiorite–granodiorite intrusions (yellow field); the fluid evolution in the Hannan South endoskarn (Mueller et al. 2012); and the evolution in Golden Mile ore bodies (this study): the oxidised Fimiston B-Lode and Oroya Flat Lode; the reduced Oroya Stage 1 Blatchford and OHW lodes; and the Oroya Stage 2 ore in the Blatchford, OHW, Phantom and Horseshoe No. 4 lodes. Buffers: hematite–magnetite (H–M), magnetite–pyrite–pyrrhotite (M–Py–Po), fayalite–magnetite–quartz (F–M–Q). **b** Log $f_{O2}$–log $f_{S2}$ diagram at 420 °C, fluid $X_{CO2}$ = 0.15, and fluid Fe in equilibrium with ferroan dolomite (activity of ankerite component 0.2 and 0.5) showing the stability fields of hematite, magnetite, siderite (activity = 0.9; ESM App. 3), pyrite and pyrrhotite in the system Fe–$CO_2$–$O_2$–$S_2$ (solid black lines), and the projected stability fields of anhydrite, calcite and dolomite–ankerite solid solution in the system Ca–Fe–$CO_2$–$O_2$–$S_2$ (dashed blue lines) relative to the isomolar $H_2S$–$HSO_4^-$ (at pH = 4–5) and $CO_2$–$CH_4$ buffers. Unit activities are used for the solid phases except carbonate. The assemblages constrain the fluid composition during deposition of the Fimiston (Fim), Oroya Stage 1 (Oro1) and Stage 2 (Oro 2) gold ore. **c** Log $f_{O2}$–log $f_{S2}$ diagram at 350 °C, fluid $X_{CO2}$ = 0.15, and fluid Fe in equilibrium with ankerite showing the expanded stability of iron-rich carbonates. Unit activities are used for the solid phases except ankerite (0.5) and siderite (0.9; ESM App. 3). The thermodynamic properties of $Fe_{0.875}S$, close in stoichiometry to Oroya pyrrhotite (ESM App. 10) are from Holland and Powell (2011)

The Oroya fluid introduced both calcium and iron (Mueller 2018) precipitating siderite + ankerite in variable proportions. In the Blatchford, OHW and parts of the No. 4 Lode, the Stage 1 high-*T* assemblage pyrite–pyrrhotite was deposited during fluid reduction by organic methane. Pyrrhotite became unstable when the fluid cooled and was partly replaced by pyrite during the deposition of siderite + ankerite. In Stage 2 ore, the presence of early pyrite + magnetite (Phantom Lode) and of late hematite and pyrite + gypsum (No. 4 Lode) indicate an oxidation state close to that of the input fluid (Fig. 12).

## Fluid oxidation state and sulfur isotopes

Sulfur isotope analyses of pyrite from major Fimiston Lodes gave $\delta^{34}S$ values of $-5.8 \pm 2.2‰$ ($n = 34$; Golding et al. 1990). Anhydrite in Fimiston breccia ore has $\delta^{34}S$ values of + 12.0 to + 19.2‰ ($n = 7$; Clout et al. 1990). Pyrite from the B-Lode and Kelly Lode has values of $-7.82 \pm 1.32‰$ ($1\sigma$, $n = 5$) and $-9.23 \pm 1.41‰$ ($1\sigma$, $n = 15$; ESM in Godefroy-Rodriguez et al. 2018). The $\Delta^{33}S$ values in pyrite from these two lodes are tightly grouped at $0.18 \pm 0.03‰$ ($1\sigma$, $n = 20$), consistent with an I-type magmatic origin for sulfur (Xue et al. 2013). In Oroya ore, $\delta^{34}S$ values of $-3.4 \pm 4.6‰$ ($n = 22$) were detected in pyrite from the oxidised Flat Lode (Golding et al. 1990), whereas the values of pyrite in the reduced Blatchford shear zone are positive and grouped into $\delta^{34}S = 0.47–1.32‰$ ($n = 5$) and $\delta^{34}S = 13.76–23.51‰$ ($n = 2$). The $\Delta^{33}S$ values ($0.55 \pm 0.12‰$, $1\sigma$, $n = 7$) of both groups indicate a contribution of black shale sulfur (Godefroy-Rodriguez et al. 2018).

The temperature-dependent $\delta^{34}S$ fractionation between sulfide and sulfate deposited from an evolved magmatic fluid with an initial bulk $\delta^{34}S$ of $2 \pm 1‰$ and molar $SO_2$–$H_2S = 1$ has been modelled by Rye (1993) taking into account the disproportionation of $SO_2$ at about 400 °C according to the reaction:

$$4SO_2 + 4H_2O = 3H_2SO_4 + H_2S \quad (2)$$

The magnitude of $\delta^{34}S$ fractionation suggests that much of the pyrite in the Fimiston Lodes and in the Flat Lode was deposited from fluids containing dissolved sulfate given temperatures of 400–350 °C (ESM Fig. 2). The pyrite analyses from pyrrhotite-bearing assemblages in the Oroya Stage 1 Blatchford shear zone show a wide spread of positive $\delta^{34}S$ values. The lower range of $\delta^{34}S = 0.47–1.32‰$ may be close to the bulk sulfur $\delta^{34}S$ of the input fluid. The upper range of $\delta^{34}S = 13.76–23.51‰$ cannot be explained by pyrite–sulfate fractionation at 400 °C (ESM Fig. 2) and may represent sulfur mobilised by the thermochemical reduction of Fimiston anhydrite, a reaction catalysed by methane:

$$CaSO_4 + CH_4 + 2H^+ = H_2S + CO_2 + Ca^{2+} + 2H_2O \quad (3)$$

## Constraints on sulfide deposition

Estimates of sulfur fugacity in the Oroya Stage 1 ore fluid forming the Blatchford and OHW lodes are based on the arsenopyrite–pyrite–pyrrhotite assemblages analysed (ESM Table 3) and on the iron content of sphalerite (Fig. 13a). When combined, these methods provide a range of log $f_{S2}$ (−5.3 to −6.6 bar). There are no independent estimates for Fimiston Lodes. Fluid evolution in the ore bodies is shown schematically in a standard log $f_{S2}$–$T$ diagram, constrained by sulfidation reactions and assuming an initial log $f_{S2} = -5.8 \pm 0.5$ bar for all fluids at a peak temperature of $420 \pm 30$ °C (grey field in Fig. 13b).

Many Fimiston Lodes (arrow F in Fig. 13b) display a simple fluid evolution path at an intermediate sulfidation state to coexisting hematite + pyrite + tennantite (red field) at lower temperature. The fluid cooling implied is consistent with the lateral zonation in the B-Lode, where As-poor pyrite + chalcopyrite dominate in the inner albite–ankerite zone, and As-rich pyrite + tennantite + chalcopyrite in the outer ankerite–phengite–quartz zone. A similar cooling path probably applies to the Oroya-style Flat Lode.

The assemblage pyrite–arsenopyrite–pyrrhotite (blue field) indicates a low to intermediate sulfidation state for the Oroya Stage 1 fluid in the reduced OHW and Blatchford lodes, whereas pyrite + chalcopyrite + tetrahedrite suggest a higher sulfur fugacity for the Oroya Stage 2 fluid (green field). In the No. 4 Lode (magenta arrow), the Oroya Stage 2 fluid remained largely in the tetrahedrite stability field but crossed temporarily into that of enargite–famatinite, before sulfur fugacity and temperature decreased during the deposition of realgar and rare native arsenic. Post-telluride deposition, the Stage 2 fluid became depleted in most metals and evolved to a high sulfidation state in the sense of Einaudi et al. (2003) precipitating trace bornite, digenite and covellite (violet arrow and field in Fig. 13b).

## Constraints on telluride deposition

Myrmekitic aggregates of altaite + native tellurium in Oroya Stage 2 ore on the Paringa South shaft 4 and 10 levels (Mueller and Muhling 2019) represent immiscible melt droplets deposited at high fluid temperature (> 400 °C) and tellurium fugacity (Fig. 13c). The Stage 2 ore in the OHW and Blatchford lodes on levels 7 and 11 does not contain native tellurium, and myrmekite is absent except for limited calaverite–petzite exsolution (Fig. 9d). Altaite, tellurantimony, calaverite and, probably, montbrayite and petzite were deposited at about 400 °C when tellurium fugacity remained above the calaverite–gold boundary, constrained in sulfur fugacity by the pyrrhotite–pyrite phase boundary and by the absence of stibnite and galena (grey field in Fig. 13c). As the fluid

cooled to 350 °C, deposition of the above tellurides continued but was accompanied by that of native gold, coloradoite and melonite (Fig. 13d). In the No. 4 and Phantom lodes, late-stage hessite and sylvanite were deposited at 350–300 °C when tellurium fugacity declined further. The absence of galena and stibnite in the OHW and Blatchford lodes and their rarity in the No. 4 and Phantom lodes suggest a rapid depletion of lead and antimony in the Stage 2 fluid due to the early crystallisation of altaite, tellurantimony and tetrahedrite. The high Au/Ag ratio (3.8–6.9) of Oroya Stage 2 ore in the Paringa South mine relative to such ore in the No. 4 Lode (Au/Ag = 1.4) reflects silver under-saturation in the fluid at 400–350 °C,

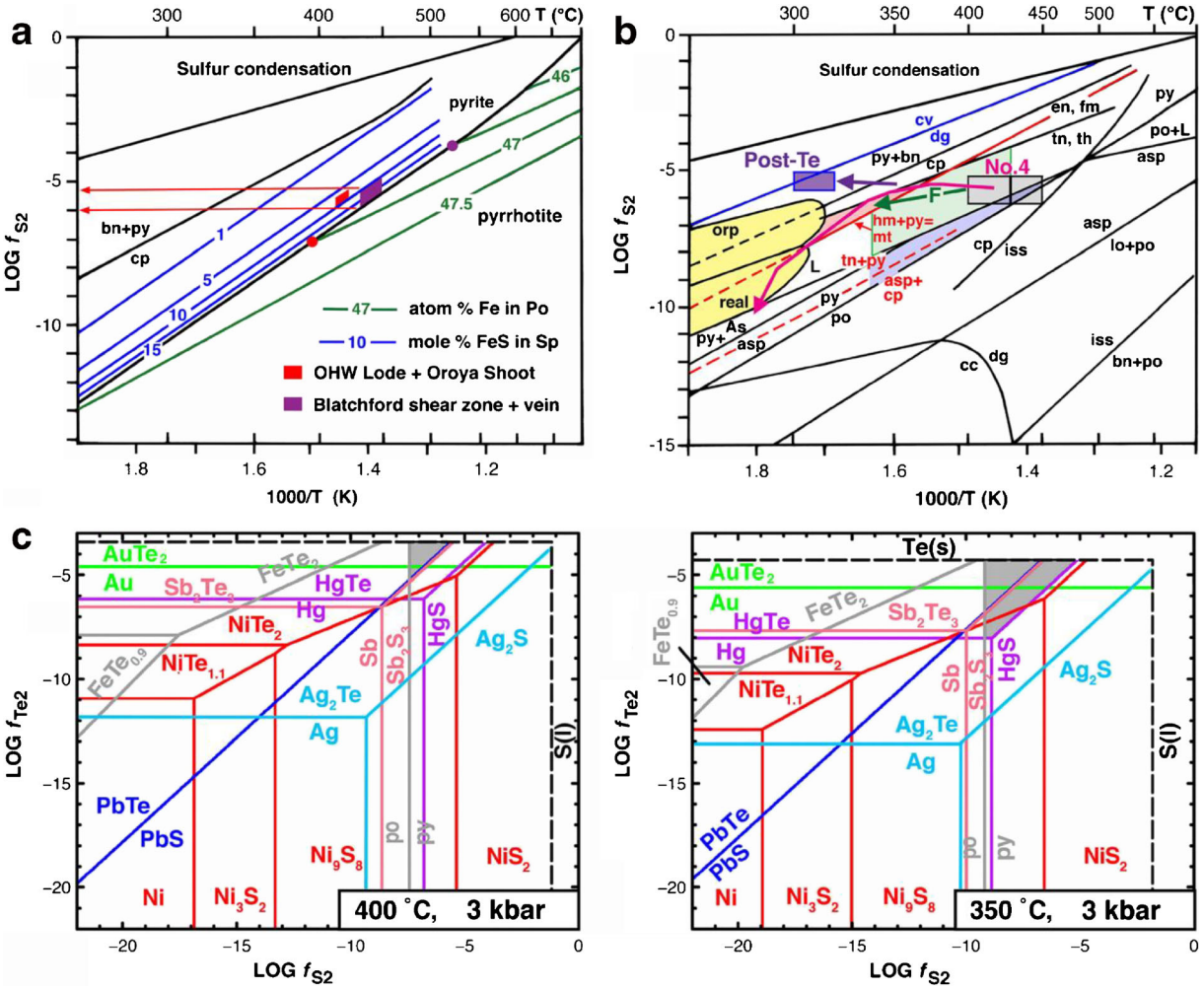


**Fig. 13** Log $f_{S2}$–$T$ and log $f_{Te2}$–log $f_{S2}$ fugacity diagrams constraining the composition of the Fimiston and Oroya hydrothermal fluids, Golden Mile, Kalgoorlie. **a** Log $f_{S2}$ –$T$ diagram at 1 bar standard state (modified from Barton and Skinner 1979; Bowles et al. 2011) showing the sulfur fugacity indicated by the Fe content of sphalerite in contact with pyrite ± pyrrhotite in Oroya-style ore (ESM App. 9 and 10). The iron content is corrected for 250 MPa pressure (Scott 1983) and plotted in windows defined by arsenopyrite thermometry (ESM Table 3). **b** Log $f_{S2}$–$T$ diagram at 1 bar standard state (modified from Barton and Skinner 1979; Einaudi et al. 2003) illustrating the evolution of sulfur fugacity based on mineral assemblages in Fimiston (red), Oroya Stage 1 (black) and Oroya Stage 2 ore (blue reactions). The peak temperature and sulfur fugacity of the Oroya fluid (grey box) are taken as the starting point for cooling. Fimiston (F) cooling path: hematite (hm) + pyrite (red field) replace magnetite (mt). The Oroya Stage 1 (blue field) and Stage 2 (green field) paths evolve post-telluride to digenite (dg) + covellite (cv; violet field). No. 4 Lode Stage 2 path: tetrahedrite–tennantite (th, tn) ± famatinite–enargite (fm, en) evolve to realgar (real) and native arsenic (As). Abbreviations: arsenopyrite (asp), bornite (bn), chalcocite (cc), chalcopyrite (cp), intermediate solid solution (iss), liquid (L), loellingite (lo), orpiment (orp), pyrrhotite (po), pyrite (py). **c** Log $f_{Te2}$–Log $f_{S2}$ diagrams at 300 MPa (3 kbar) pressure illustrating the deposition of tellurium–altaite melt droplets and crystalline grains of telluride and native gold at 400 and 350 °C during Oroya Stage 2 in the OHW and Blatchford lodes, constrained in sulfidation state by pyrrhotite–pyrite and by the absence of galena and stibnite (grey field). Late hessite in the Horseshoe No. 4 and Phantom lodes was deposited when the tellurium fugacity declined. The thermodynamic data are from Afifi et al. (1988a), and from Klein and Bach (2009) for nickel sulfide–telluride relations

and increasing Ag–telluride deposition during cooling to 300 °C. Hessite–sylvanite myrmekite in the Phantom Lode (Baker 1958) is interpreted to have formed from a high-*T* phase by solid-state exsolution at 170 °C during terrane uplift (see Cabri 1965).

## Gold transport and deposition

Previous studies of Archean ore fluids have emphasised the role of the Au $(HS)_2^-$ complex in transport, and the role of wall-rock sulfidation as the main depositional mechanism (Mikucki and Groves 1990; Mikucki 1998; Goldfarb et al. 2005). These conclusions are re-examined in the light of the pressure estimate (300 MPa) and temperature range (420–300 °C) for ore formation established in this study.

In the case of the refractory Fimiston ore, our fluid modelling confirms the dominant role of gold thio-sulfide complexes in transport (Fig. 14) and of wall-rock sulfidation in the precipitation of auriferous pyrite. During fluid infiltration, ankerite + pyrite replaced chlorite and phengite + quartz replaced albite in propylitic Golden Mile Dolerite, a process approximated by the reaction:

$$3FeO_{(chlorite)} + 6NaAlSi_3O_8 + 2Au(HS)_2^- + 2H_2S_{(aq)} + 2\,K^+_{(aq)} = 3FeS_2 + 2Au^0 + 2KAl_3Si_3O_{10}(OH)_2 + 12SiO_2 + 6Na^+_{(aq)} + 2H_2O + 0.5O_2 \quad (4)$$

Assuming a high oxidation state and neutral pH for the Fimiston input fluid, the modelling indicates steep declines in the solubility of gold, silver, tellurium and sulfur from 420 to 350 °C, suggesting that fluid cooling aided gold and telluride deposition during pyrite growth. While $H_2S_{(aq)}$ was the dominant sulfur species in the fluid, significant amounts of sulfate were present at $T > 350$ °C (Fig. 14).

These conclusions also apply to the refractory pyrite ore of the oxidised Oroya-style Flat Lode formed by fault-fill and

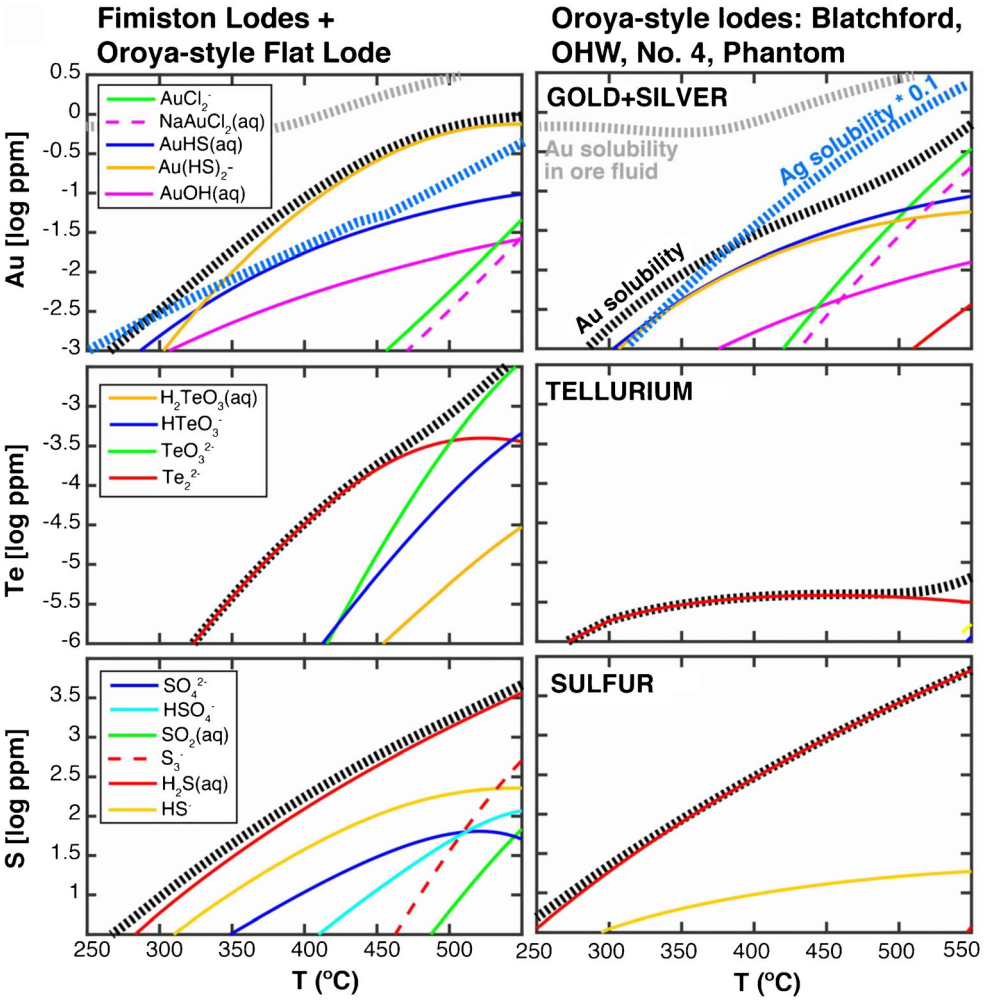


**Fig. 14** Total solubility of Au, Ag, Te and S (bold broken lines) at 300 MPa as a function of temperature in Golden Mile ore fluids (5 wt% NaCl; $X_{CO2} = 0.15$; 0.05 wt% S), modelled using the assemblages gold–calaverite and hessite–argentite under rock-buffered conditions for: (1) refractory ore in Fimiston Lodes and the Oroya-style Flat Lode (K-feldspar–quartz–muscovite + pyrite–hematite; pH 5.6 at 400 °C) in propylitic Golden Mile Dolerite; and (2) free-milling Oroya-style ore (albite–quartz–paragonite + pyrrhotite–pyrite–magnetite; pH 4.6 at 400 °C) replacing ankerite-rich wall rock. Total gold solubility under fluid-buffered conditions (assuming $X_{SO2} \sim X_{H2S}$ at 500 °C) is plotted for reference (bold grey broken line). The solubility of $AgCl_2^-$, the only significant complex at the above conditions (Pokrovski et al. 2013), has been divided by 10 and is shown at maximum relative values for comparison with gold solubility. The thermodynamic properties of the aqueous species are from Akinfiev and Zotov (2001, 2010) for gold, Mei et al. (2014) for $NaAuCl_2(aq)$ and McPhail (1995) and Grundler et al. (2013) for tellurium

replacement of propylitic GMD. The free-milling Oroya-style ore in the other lodes (OHW, Blatchford, No. 4, Phantom) replaced rocks previously altered to ankerite-rich assemblages thus excluding wall-rock carbonation–sulfidation as the principal cause of gold precipitation. Assuming reduced and acidic fluid conditions during ore deposition, the modelling indicates lower gold and tellurium solubility relative to a "Flat Lode input fluid", slightly higher silver and sulfur solubility, and an absence of dissolved sulfate (Fig. 14). Fluid cooling from 420 to 300 °C and reduction are regarded as the main mechanisms for gold, sulfide and telluride deposition.

The tellurium solubilities predicted are low (< 1 ppm). The thermodynamic properties are extrapolated from room temperature in the case of telluride and poly-telluride complexes and from experiments at < 350 °C for tellurite oxy-complexes (McPhail 1995; Grundler et al. 2013). However, the stability of poly-telluride complexes (probably $Te_2^{2-}$) has been established experimentally to 600 °C and 80 MPa (Brugger et al. 2012) suggesting that the predictions are reasonable.

## Comparison to Cenozoic gold deposits

The Golden Mile has been interpreted as an orogenic gold deposit formed in faulted greenstones from reduced metamorphic fluids generated in the lower continental crust during fold-belt evolution (Goldfarb et al. 2005; Groves et al. 2016). A challenge to this genetic model is the V-rich Oroya-style Au–Ag–Te ore, which accounts for 250–350 t of the total gold produced but is absent in most other orogenic deposits. The progression from early sulfide- to late telluride-rich ore is common in Cenozoic Au–Ag–Te deposits (Afifi et al. 1988b), an evolution recognised as Stage 1 and 2 in Oroya-style ore.

The Cenozoic deposit selected for comparison is Porgera in Papua New Guinea (651 t Au to 2018; ESM App. 1). The deposit is centred on hornblende–feldspar porphyry stocks marking a 5-km-wide magnetic anomaly interpreted as the source pluton (Richards 1990). The stocks were emplaced at 6 Ma into Cretaceous black siltstones of the Central Range, a 1300-km-long fold and thrust belt formed by the collision of the Australian continent with an island arc terrane 8 Ma ago (van Ufford and Cloos 2005). Apatite fission track ages constrain the onset of orogenic uplift at the mine to 4–5 Ma suggesting that 3–4 km of crust was eroded at a minimum rate of 0.7 km/Ma (Weiland and Cloos 1996). The stocks vary from alkali olivine gabbro to hornblende–biotite monzodiorite (Richards 1990; nomenclature after Wimmenauer 1985). The mafic phenocrysts (Mg-hastingsite > diopsidic augite) in monzodiorite have a sodic component (2–7 mol%) and are zoned from Cr–Ni-rich cores to Ti-rich rims. Alkaline indicator minerals are absent but the whole-rock Nb/Y ratios (3.3–4.5) suggest an alkaline component. $K_2O$ (1.15–2.27 wt%), Cr (6–170 ppm), Ni (8–59 ppm) and V (197–292 ppm) are enriched. The hybrid calc-alkaline/alkaline magmas are interpreted as sourced from metasomatised mantle lherzolite (Richards 1990).

The $^{40}Ar/^{39}Ar$ ages of magmatic biotite, hydrothermal biotite and roscoelite average 5.95 ± 0.17 Ma (Ronacher et al. 2002). Early alteration in monzodiorite includes sub-solidus albitisation of groundmass feldspar and a pervasive propylitic overprint (Richards 1990; Richards and Kerrich 1993). Subsequent gold-related alteration styles include (1) early calcite–magnetite veins with actinolite–biotite selvages and accessory chalcopyrite, pyrrhotite and pyrite; (2) main-stage "Waruwari" calcite–siderite–quartz veins, texture-destructive sericite–dolomite replacement, disseminated arsenical pyrite, vein-fill pyrite, sphalerite, galena and tetrahedrite; and (3) late-stage breccia and veins controlled by the Roamane fault zone, cemented and filled with chalcedony, quartz, roscoelite (29–30 wt% $V_2O_3$), calcite, dolomite, anhydrite, hematite, pyrite, chalcopyrite, tetrahedrite, gold, calaverite, krennerite, petzite, hessite, coloradoite and altaite (Richards and Kerrich 1993; Ronacher et al. 2004). Pre-mining grades were as follows: Waruwari refractory pyrite ore at 3.6 g/t Au + 14.4 g/t Ag and Roamane ore at 6 g/t Au + 9 g/t Ag including Au–Te–V ore at 35 g/t Au + 55 g/t Ag. All ore was low in base metals (0.04–0.4%; Fleming et al. 1986).

The aqueous fluids (0.1–3.1 mol% $CO_2$) trapped in vein quartz were of moderate salinity (4–10 wt% $NaCl_{eq}$) and density (0.52 g/cm$^3$). Saline (16–32 wt% $NaCl_{eq}$) and vapour-rich fluid inclusions were rare. Fluid temperatures are estimated at 350–450 °C during early propylitic and actinolite–biotite alteration, 300–350 °C during main-stage sericite–dolomite alteration and 140–260 °C during late silica–roscoelite fault-fill assuming 30–45 MPa pressure (Richards and Kerrich 1993; Richards et al. 1997; Ronacher et al. 2000, 2002, 2004). The sulfur isotope ratios of pyrite from propylitic and sericitic alteration ($\delta^{34}S$ = 1.4–5.2‰) suggest deposition from reduced magmatic fluids (bulk $\delta^{34}S$ = 4‰), whereas those of pyrite ($\delta^{34}S$ = − 14.0 to − 11.4‰) and anhydrite ($\delta^{34}S$ = 20.6–22.2‰) in Au–Te ore indicate oxidising conditions. Other isotope data ($\delta^{18}O$, δD, $\delta^{13}C$) support a magmatic fluid source for the early refractory ore and fluid mixing with groundwater during late Au–Te–V mineralisation in the Roamane Fault (Richards and Kerrich 1993).

## Summary and conclusions

The key results of previous contributions to the Golden Mile thematic issue, mainly those related to ore bodies in the

Paringa South mine, are integrated with the conclusions drawn from this study to provide a summary for comparison with the Porgera case history.

1. The Golden Mile deposit (1893–2018: 1767 t Au) is located in the Eastern Goldfields Province of the Yilgarn Craton, a continental-margin orogen characterised by 2.73–2.60 Ga granite–greenstone terranes including the Kalgoorlie ultramafic–mafic volcanic rift and the Kurnalpi andesite arc.
2. Deformation at 2680–2640 Ma took place in phases as the far-field principal stress changed from an ENE–WSW direction during D1 and D3 folding, first to the southeast during sinistral transcurrent faulting (D2), and later to the northeast during dextral faulting (D4). Such a dynamic regime is recorded in the Andean continental margin caused by periods of orthogonal and oblique subduction.
3. The deposit is controlled by the D2 Boulder Lefroy–Golden Mile fault system (> 2200 t Au). Extensive shear-zone networks of Riedel geometry formed in the Golden Mile when kilometer-scale sinistral strike-slip on the master faults strained folded GMD and PB. At 2675 Ma, granodiorite porphyry dykes were emplaced into the shear zones after D1 greenschist-facies metamorphism but prior to hydrothermal activity.
4. At 2665–2645 Ma, I-type hornblende monzodiorite and granodiorite stock–dyke complexes were emplaced into the D2 fault system in spatial association with kersantite dykes, Cu–Au skarns and mesothermal gold deposits. The calc-alkaline intrusions are enriched in lithophile (K, Rb, Li, Sr) and siderophile elements (Mg, Cr, Ni, V), a signature attributed to the melting of metasomatised mantle peridotite. Sub-solidus albitisation of plagioclase is widespread. Hornblende and apatite compositions indicate that the melts were water-rich (5–6 wt% $H_2O$), oxidised (δNNO + 1.0 to + 2.4 log units) and anhydrite bearing. The isotope composition ($\delta^{13}C_{PDB} = -3.0$ to $-2.2$‰, $\delta^{18}O_{SMOW} = 8.3$ to 9.7‰) of the magmatic $H_2O$–$CO_2$ fluids released is constrained by data from Cu–Au skarn, the Oroya kersantite dyke and local monzodiorite–granodiorite stocks.
5. In the Golden Mile, magmatic–hydrothermal fluids infiltrated the reactivated D2 fault system during the emplacement of monzodiorite porphyry dykes, generating kilometer-scale zones of pre-sulfide chlorite–calcite–epidote and sericite–ankerite ± chloritoid alteration centred on the master faults and the GMD–PB contact in the D1 Kalgoorlie Anticline. Fimiston-style ore was deposited in D2 faults during post-porphyry sinistral strike-slip (≤ 30 m offset at granodiorite dykes). Oroya-style ore associated with late kersantite dykes overprints Fimiston ore in many D2 faults but is the only ore type in D3 reverse faults, which displace the older structures up to 50 m indicating a hiatus in hydrothermal activity.
6. The Fimiston and Oroya hydrothermal fluids were aqueous–carbonic ($X_{CO2} = 0.15$), low to moderate in salinity (1.0–5.5 wt% $NaCl_{eq}$) but of high density (0.75–0.95 g/cm$^3$), trapped in quartz at a lithostatic pressure of 300 MPa (3 kbar) at 10 km crustal depth. The calculated fluid oxygen isotope ratios (8.2 to 9.8‰) are consistent with I-type magmatic water, but the carbon isotope ratios are $^{13}C$-enriched ($\delta^{13}C_{PDB} = -1.7$ to $-0.5$‰), perhaps due to the partial reduction of $CO_2$ to $CH_4$ by fluid interaction with ferrous greenstones close to the source intrusions. Such a source is indicated by the initial $^{87}Sr/^{86}Sr$ ratios of scheelite, tourmaline and anhydrite (0.7013–0.7018), which match those of monzodiorite porphyry and kersantite (0.7014–0.7018) but are higher than those of the tholeiitic host rocks (0.7009–0.7011).
7. Fimiston ore bodies (7.0 g/t Au, Au/Ag = 3.1, Cu + Zn + Pb < 0.05 wt%) in propylitic GMD account for 80–85% of the total gold. They are zoned from albite–ankerite selvages on fault-fill veins to outer hydrolytic ankerite–phengite–quartz replacement. Early pyrite + magnetite is overprinted by pyrite + hematite ± anhydrite. Much of the pyrite is arsenical, associated with chalcopyrite and tennantite, and contains submicron inclusions of native gold and tellurides. Mass balances indicate that the ore fluid introduced K, Ca, $CO_2$, S, Ba, Rb, Cs and Sr but not iron suggesting a felsic (granodiorite?) source.
8. Chlorite thermometry indicates that the Fimiston-style ore formed at 400–350 °C, well above the ambient temperature in the greenstone belt (about 250 °C). The fault-focussed ore fluid, buffered in oxidation state by magmatic $SO_2$ and $H_2S$, interacted with propylitic chlorite in the wall rock by carbonation and sulfidation. Gold was deposited in pyrite due to the destabilisation of gold thiosulfide, a process assisted by the decline in gold, silver, tellurium and sulfur solubility as the fluid cooled. The alteration of chlorite to ankerite + pyrite at the replacement front released hydrogen ions for the synchronous alteration of propylitic albite to phengite + quartz. When wall-rock interaction waned, hematite and anhydrite were deposited, recorded in pyrite by negative $\delta^{34}S$ values (− 10 to − 5‰).

9. Oroya ore bodies are subdivided into the oxidised Flat Lode (late pyrite–hematite), characterised by refractory ore (5 g/t Au) in propylitic GMD, and reduced lodes (30–120 g/t Au, Au/Ag = 1.4–6.9, Cu + Zn + Pb < 0.1 wt%, V ≤ 0.24%) such as the Oroya Shoot (> 62 t Au). Oroya-style ore is characterised by Stage 1 chalcedonic silica–siderite–chlorite replacement of ankerite-rich wall rocks, and As–Zn-rich sulfide ore composed of pyrite (15 vol%), minor pyrrhotite, arsenopyrite, sphalerite, chalcopyrite and free gold. Stage 2 ore is composed of pyrite (5%), minor magnetite, tetrahedrite, native gold and an Sb–Pb-rich suite of tellurides and sulfosalts. The ore fluid introduced silica and iron and lesser Mg, Mn, Ca, K, $CO_2$, S, Te, Li, Rb, Sr, W, Cr, Ni and V suggesting a mafic (monzodiorite?) source.
10. Arsenopyrite and chlorite thermometry indicate that the Oroya fluid infiltrated reactivated D2 faults and early D3 faults at 420 ± 30 °C and cooled to 300 °C, the magnitude of cooling constrained by late realgar. Rapid cooling, an acidic fluid and the retrograde solubility of wall-rock ankerite facilitated Stage 1 chalcedony–pyrite replacement and the subsequent deposition of siderite + chlorite (at 350 °C). In some faults, the ore fluid was reduced by trapped organic methane stabilising pyrite + pyrrhotite and acting as a catalyst in the dissolution of Fimiston anhydrite (pyrite $\delta^{34}S = +13.8$ to $+23.5‰$). Fluid interaction with carbonaceous greywacke and shale is indicated by a component of sedimentary sulfur in Stage 1 pyrite ($\Delta^{33}S = 0.5‰$). The sulfur fugacity of the $H_2S$-rich fluid is estimated at $\log f_{S2} = -5.8 \pm 0.5$ bar (at 420 °C) based on arsenopyrite and sphalerite compositions.
11. Oroya Stage 2 Au–Te ore fills veins and cements breccia crosscutting Stage 1 replacement. Quartz, chalcedony, dolomite–ankerite, calcite, V-muscovite (≤ 14 wt% $V_2O_3$), V-tourmaline and V-chlorite form the gangue of pyrite–telluride ± magnetite ± nolanite ore. Myrmekitic altaite–tellurium aggregates trapped as Pb–Te (Au–Ag) melt droplets were deposited at ≥ 400 °C together with free grains of altaite, tellurantimony, calaverite and, probably, montbrayite and petzite. As fluid temperature and tellurium fugacity declined, grains of native gold, krennerite, coloradoite and melonite also crystallised, joined by sylvanite and hessite below about 350 °C. After telluride mineralisation, the fluid evolved to a high sulfidation state ($\log f_{S2} = -5$ bar at 300 °C) depositing trace bornite and covellite + digenite.

The Archean Golden Mile and the Miocene Porgera gold deposits share the plate-tectonic setting and the relation to mantle-derived monzodiorite-suite intrusions, a fluid source responsible for the distinctive Te–V signature of late high-grade ore. They differ in the depth of formation, 10 versus 3–4 km below the surface, the difference in pressure (300 versus ≤ 100 MPa) evident in the higher $CO_2$ content ($X_{CO2} = 0.15$) and density (0.75–0.95 g/cm$^3$) of the Golden Mile fluids relative to those at Porgera ($X_{CO2} \leq 0.03$; 0.52 g/cm$^3$). In both deposits, the bulk of the gold was deposited at 450–300 °C in refractory pyrite during the carbonation–sulfidation of propylitic chlorite in the wall rocks. Cooling due to groundwater influx into the Roamane Fault at Porgera was not replicated in the deeper Golden Mile, where silica replacement formed at 10 km depth in ankerite-rich rocks due to the temperature difference between fluid and wall rock (≥ 150 °C) and the retrograde solubility of ankerite. In both deposits, late-stage pyrite–hematite ± anhydrite assemblages closely reflect the oxidation–sulfidation state of the magmatic input fluid.

**Acknowledgements** The senior author is grateful to Greg Hall and Patrick Verbeek for allowing access to the Paringa South underground mine in 1986–1987; Marco Einaudi for sharing his knowledge on magmatic–hydrothermal ore deposits during post-doctoral studies at Stanford University in 1992–1994; the staff of Kalgoorlie Consolidated Gold Mines for guided tours in 2016; the Geological Survey of Western Australia for access to the Joe Lord core library in 2016 and 2019; and the staff of the Western Australian Museum for access to their mineral collection. Malcolm Roberts acknowledges the support from the Centre for Microscopy, Characterization and Analysis (CMCA) at the University of Western Australia.

## References

Afifi AM, Kelly WC, Essene EJ (1988a) Phase relations among tellurides, sulphides and oxides: I. Thermochemical data and calculated equilibria. Econ Geol 83:377–394

Afifi AM, Kelly WC, Essene EJ (1988b) Phase relations among tellurides, sulphides and oxides: II. Applications to telluride-bearing ore deposits. Econ Geol 83:395–404

Akinfiev NN, Zotov AV (2001) Thermodynamic description of chloride, hydrosulfide and hydroxo complexes of Ag (I), Cu (I) and Au (I) at temperatures of 25-500°C and pressures of 1-2000 bar. Geochem Int 39:990–1006

Akinfiev NN, Zotov AV (2010) Thermodynamic description of aqueous species in the system Cu-Ag-Au-S-O-H at temperatures of 0-600°C and pressures of 1-3000 bar. Geochem Int 48:714–720

Baker G (1958) Tellurides and selenides in the Phantom Lodes, Great Boulder mine, Kalgoorlie. Australasian Inst Min Metall, Melbourne, Stillwell Anniversary Volume, pp 15-40

Barton PB, Skinner BJ (1979) Sulfide mineral stabilities. In: Barnes HL (ed) Geochemistry of hydrothermal ore deposits, 2nd edn. Wiley, New York, pp 278–403

Barton MD, Seedorff E, Ilchik RP, Ghidotti G (1997) Contrasting siliceous replacement mineralization, east-central Nevada. In: Vikre P, Thompson TB, Bettles K, Christensen O, Parratt R (eds) Carlin-type gold deposits field conference. SEG guidebook series, vol. 28, pp. 131–134

Bartram GD, McCall GJH (1971) Wall-rock alteration associated with auriferous lodes in the Golden Mile, Kalgoorlie. In: Glover JE (ed) Symposium on Archaean rocks. Geol Soc Australia, Publ 3, pp 191–199

Bath LB, Walshe JL, Cloutier J, Verrall M, Cleverley JS, Pownceby MI, Macrae CM, Wilson NC, Tunjic J, Nortje GS, Robinson P (2013) Biotite and apatite as tools for tracking pathways of oxidized fluids in the Archean East Repulse gold deposit, Australia. Econ Geol 108: 667–690

Bindi L, Paar WH, Lepore GO (2018) Montbrayite, (Au,Ag, Sb,Pb, $Bi)_{23}(Te,Sb,Pb,Bi)_{38}$, from the Robb-Montbray mine, Montbray, Quebec: crystal structure and revision of the chemical formula. Can Mineral 56:129–142

Bowles JFW, Howie RA, Vaughan DJ, Zussman J (2011) Rock-forming minerals, non-silicates: oxides, hydroxides and sulphides, 2nd edn, vol 5A. The Geological Society, London

Braun E, Raith M (1985) Fe-Ti-oxides in metamorphic basites from the Eastern Alps, Austria: a contribution to the formation of solid solutions of natural Fe-Ti-oxide assemblages. Contrib Mineral Petrol 90: 199–213

Brugger J, Etschmann B, Grundler P, Liu W, Testemale D, Pring A (2012) XAS evidence for the stability of polytellurides in hydrothermal fluids up to 599°C, 800 bar. Am Mineral 97:1519–1522

Bucher K, Frey M (2002) Petrogenesis of metamorphic rocks, 7th edn. Springer, Berlin, 341 pp

Cabri LJ (1965) Phase relations in the Au-Ag-Te system and their mineralogical significance. Econ Geol 60:1569–1606

Cathelineau M (1988) Cation site occupancy in chlorites and illites as a function of temperature. Clay Miner 23:471–485

Chang LLY, Howie RA, Zussman J (1998) Non-silicates: sulphates, carbonates, phosphates, halides. In: Rock-forming minerals, 5B, 2nd edn. The Geological Society, London

Clout JMF (1989) Structural and isotopic studies of the Golden Mile gold-telluride deposit, Kalgoorlie, Western Australia. Dissertation, Monash University, Clayton, 352 pp

Clout JMF, Cleghorn JH, Eaton PC (1990) Geology of the Kalgoorlie goldfield. In: Hughes FE (ed) Geology of the mineral deposits of Australia and Papua New Guinea. Melbourne, Australasian Inst Min Metall, Monograph 14, pp 411–431

Deer WA, Howie RA, Zussman J (1992) An introduction to the rock-forming minerals, 2nd edn. Longman House, Burnt Mill

Dick JM (2008) Calculation of the relative metastabilities of proteins using the CHNOSZ software package. Geochem Trans 9:17

Einaudi MT, Hedenquist JW, Inan EE (2003) Sulfidation state of fluids in active and extinct hydrothermal systems: transitions from porphyry to epithermal environments. SEG Special Publ 10:285–313

Evans KA, Phillips GN, Powell R (2006) Rock-buffering of auriferous fluids in altered rocks associated with the Golden Mile-style mineralization, Kalgoorlie Gold Field, Western Australia. Econ Geol 101: 805-817

Fleet ME (2003) Sheet silicates: micas, rock-forming minerals, 3A. 2nd edn. The Geological Society, London

Fleming AW, Handley GA, Williams KL, Hills AL, Corbett GJ (1986) The Porgera gold deposit, Papua New Guinea. Econ Geol 81:660–680

Fournier RO (1985) The behaviour of silica in hydrothermal solutions. Rev Econ Geol 2:45–61

Gauthier L, Hagemann S, Robert F (2007) The geological setting of the Golden Mile gold deposit, Kalgoorlie, W.A. In: Bierlein FP, Knox-Robinson CM (eds) Kalgoorlie 2007, old ground, new knowledge, abstracts. Geoscience Australia, Record 2007/14, pp 181–185

Godefroy-Rodriguez M, Hagemann S, LaFlamme C, Fiorentini M (2018) The multiple sulfur isotope architecture of the Golden Mile and Mt Charlotte deposits, Western Australia. Miner Deposita online, https://doi.org/10.1007/s00126-018-0828-y, this issue

Goldfarb RJ, Baker T, Dubé B, Groves DI, Hart CJR, Gosselin P (2005) Distribution, character and genesis of gold deposits in metamorphic terranes. Econ Geol 100th Anniversary Volume, pp 407–450

Golding LY (1978) Mineralogy, geochemistry and origin of the Kalgoorlie gold deposits, Western Australia. Dissertation, The University of Melbourne, 402 pp

Golding SD, Wilson AF (1983) Geochemical and stable isotope studies of the No. 4 Lode, Kalgoorlie, Western Australia. Econ Geol 78: 438–450

Golding SD, Groves DI, McNaughton NJ, Mikucki EJ, Sang JH (1990) Sulphur isotope studies. In: Ho SE, Groves DI, Bennett JM (eds) Gold deposits of the Archaean Yilgarn block, Western Australia: nature, genesis, and exploration guides. University of Western Australia, Publ 20, pp 259–262

Groves DI, Goldfarb RJ, Santosh M (2016) The conjunction of factors that lead to formation of giant gold provinces and deposits in non-arc settings. Geosci Front 7:303–314

Grundler PV, Brugger J, Etschmann BE, Helm L, Liu W, Spry PG, Tian W, Testemale D, Pring A (2013) Speciation of aqueous tellurium (IV) in hydrothermal solutions and vapours, and the role of oxidized tellurium species in Te transport and gold deposition. Geochim Cosmochim Acta 120:298–325

Gustafson JK, Miller FS (1937) Kalgoorlie geology re-interpreted. Proc Aust Inst Min Metall 106:93–125

Ho SE, Bennett JM, Cassidy KF, Hronsky JMA, Mikucki EJ, Sang JH (1990) Fluid inclusion studies. In: Ho SE, Groves DI, Bennett JM (eds) Gold deposits of the Archaean Yilgarn block, Western Australia: nature, genesis, and exploration guides. University of Western Australia, Publ 20, pp. 198–211

Holland TJB, Powell R (2000) AX—a program to calculate activities of mineral end members from chemical analyses (usually determined by electron microprobe): http://www.esc.cam.ac.uk/astaff/holland/ax.html

Holland TJB, Powell R (2011) An improved and extended internally consistent thermodynamic dataset for phases of petrological interest, involving a new equation of state for solids. J Metamorph Geol 29: 333–383

International Mineralogical Association, IMA (1999) Nomenclature of the micas. Mineral Mag 63:267–279

Klein F, Bach W (2009) Fe-Ni-Co-O-S phase relations in peridotite-seawater interactions. J Petrol 50:37–59

Kretschmar U, Scott SD (1976) Phase relations involving arsenopyrite in the system Fe-As-S and their application. Can Mineral 14:364–386

Laird J (1988) Chlorites: metamorphic petrology. In: Bailey SW (ed) Hydrous phyllosilicates (exclusive micas). Rev Mineralogy 19: 405–453

Lanari P, Wagner T, Vidal O (2014) A thermodynamic model for di-trioctahedral chlorite from experimental and natural data in the system $MgO-FeO-Al_2O_3-SiO_2-H_2O$: applications to P-T sections and geothermometry. Contrib Mineral Petrol 167:968

Lin JC, Hsieh KC, Sharma RC, Chang YA (1989) The Pb-Te (lead-tellurium) system. Bull Alloy Phase Diagr 10:340–347

Manalo PC, Imai A, Subang LL, de los Santos MC, Yanagi K, Takahashi R, NJF B (2018) Mineralization of the northwest quartz-pyrite-gold veins: implications for multiple mineralization events at Lepanto, Mankayan mineral district, northern Luzon, Philippines. Econ Geol 113:1609–1626

McPhail DC (1995) Thermodynamic properties of aqueous tellurium species between 25 and 350°C. Geochim Cosmochim Acta 59: 851–866

Mei Y, Liu WH, Sherman DM, Brugger J (2014) Metal complexation and ion hydration in low density hydrothermal fluids: ab initio molecular dynamics simulation of Cu (I) and Au (I) in chloride solutions (25-1000°C, 1-5000 bar). Geochim Cosmochim Acta 131:196–212

Mikucki EJ (1998) Hydrothermal transport and depositional processes in Archean lode-gold systems: a review. Ore Geol Rev 13:307–321

Mikucki EJ, Groves DI (1990) Mineralogical constraints. In: Ho SE, Groves DI, Bennett JM (eds) Gold deposits of the Archaean Yilgarn block, Western Australia: nature, genesis, and exploration guides. University of Western Australia, Publ 20, pp. 212–220

Mikucki EJ, Ridley JR (1993) The hydrothermal fluid of Archaean lode gold deposits at different metamorphic grades: compositional constraints from ore and wallrock alteration assemblages. Miner Deposita 28:469–481

Mueller AG (1990) The nature and genesis of high- and medium-temperature Archaean gold deposits in the Yilgarn block, Western Australia, including a specific study of scheelite-bearing gold skarn deposits. Dissertation, the University of Western Australia, Perth

Mueller AG (2007) Copper-gold endoskarns and high-Mg monzodiorite-tonalite intrusions at Mt. Shea, Kalgoorlie, Australia: implications for the origin of gold-pyrite-tennantite mineralization in the Golden Mile. Miner Deposita 42:737–769

Mueller AG (2017) Structural setting of Fimiston- and Oroya-style pyrite-telluride-gold lodes, Paringa South mine, Golden Mile, Kalgoorlie: 1. Shear zone systems, porphyry dykes and deposit-scale alteration zones. Miner Deposita online, https://doi.org/10.1007/s00126-017-0747-3, this issue

Mueller AG (2018) Paragonite-chloritoid alteration in the Trafalgar Fault and Fimiston- and Oroya-style gold lodes in the Paringa South mine, Golden Mile, Kalgoorlie: 2. Muscovite-pyrite and silica-chlorite-telluride ore deposited by two superimposed hydrothermal systems. Miner Deposita online, https://doi.org/10.1007/s00126-018-0813-5, this issue

Mueller AG, Muhling JR (2019) Early pyrite and late telluride mineralization in vanadium-rich gold ore from the Oroya Shoot, Paringa South mine, Golden Mile, Kalgoorlie: 3. Ore mineralogy, Pb-Te (Au-Ag) melt inclusions, and stable isotope constraints on fluid sources. Miner Deposita online, https://doi.org/10.1007/s00126-019-00876-6, this issue

Mueller AG, Harris LB, Lungan A (1988) Structural control of greenstone-hosted gold mineralization by transcurrent shearing—a new interpretation of the Kalgoorlie mining district, Western Australia. Ore Geol Rev 3:359–387

Mueller AG, de Laeter JR, Groves DI (1991) Strontium isotope systematics of hydrothermal minerals from epigenetic Archean gold deposits in the Yilgarn block, Western Australia. Econ Geol 86:780–809

Mueller AG, Lawrance LM, Muhling J, Pooley GD (2012) Mineralogy and PTX relationships of the Archean Hannan South Au-Cu (Co-Bi) deposit, Kalgoorlie, Western Australia: thermodynamic constraints on the formation of a zoned intrusion-related skarn. Econ Geol 107: 1–24

Mueller AG, Hagemann SG, McNaughton NJ (2016) Neoarchean orogenic, magmatic and hydrothermal events in the Kalgoorlie-Kambalda area, Western Australia: constraints on gold mineralization in the Boulder Lefroy-Golden Mile fault system. Miner Deposita online, https://doi.org/10.1007/s00126-016-0665-9, this issue

Muntean JL (2018) The Carlin gold system: applications to exploration in Nevada and beyond. Rev Econ Geol 20:39–88

Ohmoto H (1986) Stable isotope geochemistry of ore deposits. Rev Mineral 16:491–559

Pokrovski GS, Roux J, Ferlat G, Jonchiere R, Seitsonen AP, Vuilleumier R, Hazemann J-L (2013) Silver in geological fluids from in situ X-ray absorption spectroscopy and first-principles molecular dynamics. Geochim Cosmochim Acta 106:501–523

Qian G, Xia F, Brugger J, Skinner WM, Bei J, Chen G, Pring A (2011) Replacement of pyrrhotite by pyrite and marcasite under hydrothermal conditions up to 220°C: an experimental study of reaction textures and mechanisms. Am Mineral 96:1878–1893

Richards JP (1990) Petrology and geochemistry of alkali intrusives at the Porgera gold deposit, Papua New Guinea. J Geochem Explor 35: 141–199

Richards JP, Kerrich R (1993) The Porgera gold mine, Papua New Guinea: magmatic hydrothermal to epithermal evolution of an alkali-type precious metal deposit. Econ Geol 88:1017–1052

Richards JP, Bray CJ, Channer DMD, Spooner ETM (1997) Fluid chemistry and processes at the Porgera gold deposit, Papua New Guinea. Miner Deposita 32:119–132

Robert F, Kelly WC (1987) Ore-forming fluids in Archean gold-bearing quartz veins at the Sigma mine, Abitibi greenstone belt, Quebec, Canada. Econ Geol 82:1464–1482

Ronacher E, Richards JP, Johnston MD (2000) Evidence for fluid phase separation in high-grade ore zones at the Porgera gold deposit, Papua New Guinea. Miner Deposita 35:683–688

Ronacher E, Richards JP, Villeneuve ME, Johnston MD (2002) Short life-span of the ore-forming system at the Porgera gold deposit, Papua New Guinea: laser $^{40}Ar/^{39}Ar$ dates for roscoelite, biotite, and hornblende. Miner Deposita 37:75–86

Ronacher E, Richards JP, Reed MH, Bray CJ, Spooner ETC, Adams PD (2004) Characteristics and evolution of the hydrothermal fluid in the North Zone high-grade area, Porgera gold deposits, Papua New Guinea. Econ Geol 99:843–867

Rye RO (1993) The evolution of magmatic fluids in the epithermal environment: the stable isotope perspective. Econ Geol 88:733–753

Scantlebury GM (1983) The characterization and origin of the gold lodes in and around the Brownhill Syncline, Golden Mile, Kalgoorlie, Western Australia. B.Sc. (Honours) thesis, the University of Western Australia, Perth

Scott SD (1983) Chemical behaviour of sphalerite and arsenopyrite in hydrothermal and metamorphic environments. Min Mag 47:427–435

Shackleton JM, Spry PG, Bateman R (2003) Telluride mineralogy of the Golden Mile deposit, Kalgoorlie, Western Australia. Can Mineral 41:1503–1524

Sharp ZD, Essene EJ, Kelly WC (1985) A re-examination of the arsenopyrite geothermometer: pressure considerations and applications to natural assemblages. Can Mineral 23:517–534

Shvarov YV (2008) HCh: new potentialities for the thermodynamic simulation of geochemical systems offered by Windows. Geochem Int 46:834–839

Simpson ES (1912) Detailed mineralogy of Kalgoorlie and Boulder with special reference to the ore deposits. In: Simpson ES, Gibson CG (eds) The geology and ore deposits of Kalgoorlie, East Coolgardie

Goldfield, Part 1. Geol Surv Western Australia, Bulletin 42, pp 77–160

Tomich SA (1952) Some structural aspects of Kalgoorlie geology. Proc Aust Inst Min Metall 164(165):45–76

Travis GA, Woodall R, Bartram GD (1971) The geology of the Kalgoorlie Goldfield. In: Glover JE (ed) Symposium on Archaean rocks. Geol Soc Australia, Publ 3, pp 175–190

Tripp G I (2013) Stratigraphy and structure in the Neoarchaean of the Kalgoorlie district, Australia: critical controls on greenstone-hosted gold deposits. Dissertation, James Cook University, Townsville

Van Ufford AQ, Cloos M (2005) Cenozoic tectonics of New Guinea. AAPG Bull 89:119–140

Vaughn ES, Ridley JR (2014) Evidence for exsolution of Au-ore fluids from granites crystallized in the mid-crust, Archaean Louis Lake batholith, Wyoming. In: Garofalo PS, Ridley JR (eds) Gold-transporting hydrothermal fluids in the Earth's crust. Geological Society, London, Special Publ 402

Voronin MV, Osadchii EG, Brichkina EA (2017) Thermochemical propertries of silver tellurides including empressite (AgTe) and phase diagrams for Ag-Te and Ag-Te-O. Phys Chem Miner 44: 639–653

Weiland RJ, Cloos M (1996) Pliocene-Pleistocene asymmetric unroofing of the Irian fold belt, Irian Jaya, Indonesia: apatite fission-track thermochronology. GSA Bull 108:1438–1449

Wimmenauer W (1985) Petrografie der magmatischen und metamorphen Gesteine. Enke, Stuttgart

Xing YL, Etschmann B, Liu WH, Mei Y, Shvarov Y, Testemale D, Tomkins A, Brugger J (2019) The role of fluorine in hydrothermal mobilization and transportation of Fe, U and REE and the formation of IOCG deposits. Chem Geol 504:158–176

Xue Y, Campbell I, Ireland TR, Holden P, Armstrong R (2013) No mass-independent sulfur isotope fractionation in auriferous fluids supports a magmatic origin for Archean gold deposits. Geology 41:791–794

Zimmer K, Zhang YL, Lu P, Chen YY, Zhang GR, Dalkilic M, Zhu C (2016) SUPCRTBL: a revised and extended thermodynamic dataset and software package of SUPCRT92. Comput Geosci 90:97–111

**Publisher's note** Springer Nature remains neutral with regard to jurisdictional claims in published maps and institutional affiliations.